

Magnetization dynamics in layered systems with coexisting bilinear and biquadratic interlayer exchange coupling

A. Bonda¹,* L. Uba¹, and S. Uba¹*Faculty of Physics, University of Białystok, K. Ciolkowskiego 1L, 15-245 Białystok, Poland*

(Received 10 June 2022; revised 24 March 2023; accepted 27 March 2023; published 6 April 2023)

Important aspects of exchange-coupled magnetic layered structures are related to the noncollinear arrangement of sublayer magnetizations which can arise from competition between bilinear (BL) and biquadratic (BQ) interlayer exchange coupling (IEC). In this work, the influence of coexisting BL and BQ IEC of different strengths on magnetization precession in layered systems is investigated both experimentally and theoretically. Laser-induced magnetization precession has been studied in the Fe/Si(d_{Si}) multilayers (MLS) as a function of the amplitude (H) and orientation angle (θ_H) of external magnetic field using time-resolved magneto-optical Kerr (TRMOKE) effect. Strongly changing characters of precession frequency dependencies $\omega(H, \theta_H)$ for Fe sublayer thickness $d_{\text{Fe}} = 3$ nm and Si spacer-layer thicknesses (d_{Si}) varying in the range of 0.9–2.4 nm have been observed. Analytical formulas for acoustic and optic mode dispersion relations with coexisting BL and BQ IEC, scaled by J_1 and J_2 parameters, respectively, for the in-plane effective magnetic anisotropy and arbitrary magnetic field direction were derived, and very good agreement with the experimentally observed frequency dependencies has been obtained. It is shown that BQ coexisting with BL IEC significantly influences on the magnitude and form of dispersion relations. From analytical formula derived, it follows that zero-field optical mode frequency tends to zero as $|J_1|$ approaches $2J_2$. The acoustic and optic mode-crossing effect has been observed and it is found that values of crossing fields and frequency gaps strongly increase as θ_H angles decrease and depend on relative BL and BQ IEC strengths. The BL IEC is of ferromagnetic type with $J_1 \approx 1.6$ mJ/m² for the MLS with $d_{\text{Si}} = 0.9$ nm, and changes to antiferromagnetic one with $J_1 \approx -0.9$ mJ/m² for the MLS with $d_{\text{Si}} = 1.4$ nm, while the J_2 parameter of BQ IEC decreases from 1.8 to 1.0 mJ/m². The coupling strengths decrease by one to two orders of magnitude for the sample with $d_{\text{Si}} = 2.4$ nm, but both mode frequencies are still observed and well reproduced by the theory. It is shown that J_1 and J_2 parameters obtained in the TRMOKE experiment coincide within the estimated error bars with the determined from independent measurements of magnetization processes in the static magneto-optical Kerr effect and interpreted with the use of analytical formulas derived. Numerical solutions of coupled Landau-Lifshitz-Gilbert (LLG) equations for acoustic and optic modes, with inclusion of BL IEC, intrinsic Gilbert damping, and spin-pumping damping terms, and extended to include BQ IEC, were performed and fitted to experimental data. It is shown that determined effective damping coefficients on H and θ_H dependencies for acoustic and optic modes are very well simulated with the use of LLG equation solutions with Gilbert damping, spin-pumping-damping-related effective spin-mixing conductance, and spin-diffusion length parameters included. The dependencies of the parameters on d_{Si} spacer-layer thickness are discussed and compared with available data for other systems.

DOI: [10.1103/PhysRevB.107.144408](https://doi.org/10.1103/PhysRevB.107.144408)

I. INTRODUCTION

The layered structures in which the exchange interaction between magnetic sublayers occurs through a nonmagnetic one are intensively studied for both fundamental and application reasons [1–3]. Many layered systems exhibit bilinear interlayer exchange coupling (BL IEC) [4–10], in which magnetic sublayer magnetizations are parallel for ferromagnetic and antiparallel for antiferromagnetic coupling, respectively. The structures, exhibiting also biquadratic interlayer exchange coupling (BQ IEC), in which magnetic sublayer magnetizations are orthogonally arranged, were less frequently examined [11–13]. However, both BL and BQ IEC are equally

important for applications in spintronics devices (see, e.g., Ref. [12] and references therein). The systems with noncollinear magnetizations alignment in which the canting angle between magnetization vectors of the sublayers differs from both 0° and 180° are important for spin-transfer torque magnetic random access memory (STT MRAM) devices. The noncollinear magnetization alignment with arbitrary canting angle can be achieved without external magnetic field in the case of simultaneous BL and BQ IEC occurrence of appropriate coupling strength's ratio. Materials with such properties are particularly interesting for spintronic applications, and recently a method for control of noncollinear IEC has been proposed by Nunn *et al.* [12] by introducing the Fe_xRu_{1-x} spacer alloy in a Co/Ru/Co trilayer.

Layered structures with interlayer exchange coupling have also attracted much attention for the use in ultrafast

*a.bonda@uwb.edu.pl

spintronics devices because the magnetization can respond at terahertz frequencies [14] and are becoming the basis of a promising nanotechnology in the field of spintronics [15,16]. Magnetization dynamics in the structures is studied also for fundamental reasons, and a rich variety of the effects was observed using different experimental methods, ranging from ferromagnetic resonance (FMR) and Brillouin light scattering (BLS) [1,4,11] to time-resolved magneto-optical Kerr effect (TRMOKE) [5,7,10,17–19]. In particular, magnetization precession can be directly observed in time domain using TRMOKE technique, and precession damping can be determined from the observed relaxation of the precession amplitude.

In the literature, there are a number of theoretical and experimental works concerning magnetization dynamics in magnetically coupled layered structures, starting from classical papers by Layadi [20,21], Layadi and Artman [22], Zhang *et al.* [4], Rezende *et al.* [11], and others. In the papers, analytical formulas for magnetization precession frequency (ω) vs magnetic field (H), i.e., dispersion relations for acoustic $\omega_{ac}(H)$ and optic $\omega_{op}(H)$ modes, were derived for BL IEC [4,20,22]. In Refs. [11,21] the dispersion relations including both BL and BQ IEC were given for the magnetic field oriented in the sample plane, when formulas simplify considerably. The theory was successfully applied to explain FMR experiments in Refs. [4,11,23]. Recently, Sud *et al.* derived analytical formulas for magnetization precession at arbitrary H -field orientation angle (θ_H), taking into account BL coupling, and applied them to explain FMR experiments in synthetic antiferromagnets (SyAF) [24].

As opposed to FMR, TRMOKE experiments are performed mostly at oblique magnetic field orientation, in which case the magnetization precession can occur through the change of effective magnetic anisotropy field induced by femtosecond laser pulses [25]. In Ref. [8], dispersion relations were derived in the case of BL IEC and applied to explain TRMOKE experiment for multiple θ_H angles in ferromagnetically coupled Fe/Pt/FePt trilayers. The BL IEC was also investigated in antiferromagnetically coupled trilayer films CoFeB/Ru/CoFeB [19], and L1₀-FePt/Ta(Pt)/[Co/Ni]₅ structures with ferromagnetic coupling [26]. Analytical formulas including both BL and BQ IEC are given for arbitrary θ_H angle in Ref. [7], but these formulas are limited to coplanar sublayer magnetizations with external magnetic field, as in the case of structure with perpendicular effective magnetic anisotropy [Ni/Co]₄/Ru/[Co/Ni]₃ [7]. However, to our knowledge, no analytical formulas including both BL and BQ IEC have been derived so far for the most complex case of in-plane effective magnetic anisotropy and arbitrary magnetic field direction.

Layered structures which are known to have simultaneous BL and BQ IEC are Fe/Si multilayers (MLS), in which both couplings can be widely changed by tuning the Si spacer-layer thickness, and which were studied using different methods [27–34]. Many interesting magnetic behaviors in Fe/Si structures have been observed and were related to the spontaneously formed iron silicide layers of different structure and composition at the interfaces [33–35]. In several works, the studies were performed using FMR and BLS as a function of magnetic field oriented in the sample plane, where both

acoustic and optic frequency modes were observed and interpreted [30,32] in terms of theory of Ref. [11].

In this paper, we report comprehensive studies of magnetization precession in Fe/Si multilayers using TRMOKE measurement technique. The motivation of this work was to investigate how the magnetization precession and magnetic damping relaxation processes in the structures, triggered by femtosecond laser pulses, depend on the magnetic field magnitude and orientation. In particular, the question was how the strong biquadratic interlayer coupling, in addition to the bilinear one of comparable magnitude, influences on the dispersion relations of the acoustic and optic frequency modes.

The aim of this work is the systematic study of the magnetization precession up to nanosecond timescale, as a function of magnitude and direction of external magnetic field, in [Fe/Si(d_{Si})]₁₅ multilayers with different Si spacer-layer thickness d_{Si} . Two distinctly different frequency modes were observed in magnetization precession $\omega_{ac,op}(H, \theta_H)$ dependencies and interpreted in terms of acoustic and optic branches. Strong influence of interlayer coupling strengths and signs on magnetization precession frequencies and damping parameters has been found.

Analytical formulas for $\omega_{ac,op}(H, \theta_H)$ functions in symmetrical trilayer structure with coexisting bilinear and biquadratic interlayer couplings were derived. The formulas reproduce very well the experimental results. The values of BL and BQ IEC, determined from TRMOKE experiment and independently from static MOKE hysteresis loops, were compared. Strong dependence of interlayer exchange coupling on Si spacer-layer thickness has been found. The coupled Landau-Lifshitz-Gilbert (LLG) equations including different damping terms were numerically solved, and the fitting procedure of the solutions to the experimental TRMOKE delay-time dependencies was performed. The Gilbert damping and spin-pumping damping parameters of magnetization precession relaxation processes for different d_{Si} were determined and discussed.

The scope of the paper is organized as follows. In Sec. II, the experimental conditions for TRMOKE measurements and other experimental details are described. In Sec. III, theoretical description and derivation of static and dynamic relations for layered structures with bilinear and biquadratic interlayer coupling are presented. The results of measurements, data analysis, and interpretation of the results in the frame of analytical dispersion relations and numerical solutions of LLG equations are presented in Sec. IV. Summary and conclusions are included in Sec. V.

II. EXPERIMENTAL DETAILS

All-optical TRMOKE method was used to investigate the laser-induced magnetization precession in Fe/Si(d_{Si}) multilayers. The measurements were carried out as a function of magnetic field magnitude up to 6.5 kOe for three different H -field angles $\theta_H = 10^\circ, 25^\circ, \text{ and } 50^\circ$ with respect to sample plane normal (Fig. 1). The femtosecond regenerative amplifier system was used as the source of the laser pulse trains, generated with repetition of 10 kHz at 800 nm wavelength with the fluences fixed at 0.05 and 1.6 mJ/cm² for the probe and pump beam, respectively. The probe and pump beams

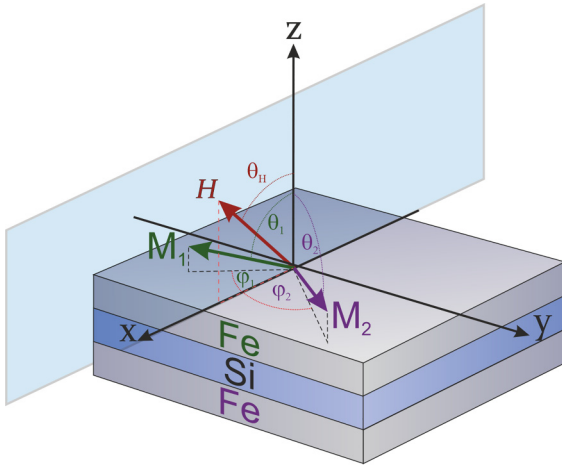


FIG. 1. Schematic illustration of trilayer structure and coordinate system used in the model (see text).

were incident on the sample at $\sim 25^\circ$ and $\sim 5^\circ$ angles with respect to the z axis, respectively, in the light incidence plane shown as shaded area in Fig. 1. The transient Kerr rotation was synchronously detected using balanced optical bridge detector in the scheme of the mechanical chopper pump beam modulation. Other key aspects of measurement technique and experimental setup used were described in details elsewhere [36,37]. Static hysteresis loops measurements were done in polar and longitudinal MOKE geometry with magnetic field magnitude up to 22 kOe using magneto-optical magnetometer setup based on the light polarization modulation technique [38–40]. All the measurements were performed at ambient temperature of 297 K.

The samples were grown and characterized at the Institute of Molecular Physics in Poznan, Poland. The Fe/Si multilayers were deposited in UHV chamber by DC magnetron sputtering onto oxidized, (001)-oriented Si substrates. The thickness of oxidized Si layer was about 100 nm. The first Fe layer was deposited directly on the top of the oxidized layer. Each sample was composed of 15 periods of (Fe/Si) bilayers. The studied samples, referred hereafter as samples S1, S2, and S3, have nominal thicknesses of Si sublayers $d_{\text{Si}} = 0.9, 1.4,$ and 2.4 nm, respectively, and for Fe sublayers d_{Fe} is fixed to 3 nm. The crystalline structure of the samples and their multilayer periodicity were examined using the high- and small-angle x-ray diffraction, respectively. The method of preparation and samples characterization are described in Refs. [41,42].

III. STATIC AND DYNAMIC RELATIONS FOR LAYERED STRUCTURES WITH COEXISTING BILINEAR AND BIQUADRATIC INTERLAYER COUPLING

For an ideal multilayer, being a repetition of successive sequences of magnetic and nonmagnetic layers, all parameters of the sublayers, except of magnetization directions in the magnetic sublayers, are identical. It is then justified to assume as a first approximation that a set of equations describing the multilayered system can be reduced to the one for a symmetrical trilayer. In the following, we will consider static and

dynamic characteristics of the symmetrical trilayer, i.e., two identical magnetic layers separated by a nonmagnetic spacer layer and magnetically coupled as a result of BL and BQ IEC.

A. Perpendicular and in-plane hysteresis loops

To derive the solutions for the $M(H)$ hysteresis loops in the case of mixed BL and BQ IEC, we will use the coordinate system with z axis perpendicular and x axis parallel to the sample plane, with the magnetic field of magnitude H oriented in the x - z plane at angle of θ_H with respect to the z axis (see Fig. 1). The free energy for the symmetrical trilayer having the shape and uniaxial magnetic anisotropy can be expressed in the spherical coordinate system in the form

$$\begin{aligned}
 E = \sum_{i=1}^2 \left\{ -HM_s[\cos(\theta_H)\cos(\theta_i) \right. \\
 \left. + \sin(\theta_H)\sin(\theta_i)\cos(\varphi_i)] + \frac{1}{2}K_u^{\text{eff}}M_s\sin^2(\theta_i) \right\} \\
 - \frac{J_1}{d}[\cos(\theta_1)\cos(\theta_2) + \sin(\theta_1)\sin(\theta_2)\cos(\varphi_1 - \varphi_2)] \\
 + \frac{J_2}{d}[\cos(\theta_1)\cos(\theta_2) + \sin(\theta_1)\sin(\theta_2)\cos(\varphi_1 - \varphi_2)]^2,
 \end{aligned} \tag{1}$$

where d is the thickness of magnetic sublayers, and θ_i and φ_i are polar and azimuthal angles of magnetization vectors \mathbf{M}_i of different orientations, but the same magnitude M_s . The first two lines in Eq. (1) represent Zeeman and effective magnetic anisotropy energy. The K_u^{eff} represents the uniaxial and shape anisotropies and is related to the effective anisotropy field $H^{\text{eff}} = 2K_u/M_s - 4\pi M_s$. The J_1 and J_2 are the BL and BQ interlayer coupling parameters, respectively, which scale the interlayer exchange-coupling energy and are related to the exchange-coupling fields $H_{\text{ex}}^{(1)} = J_1/(M_s d)$ and $H_{\text{ex}}^{(2)} = J_2/(M_s d)$. Note that $H_{\text{ex}}^{(1)} > 0$ and $H_{\text{ex}}^{(1)} < 0$ correspond to ferromagnetic and antiferromagnetic arrangements, respectively, and $H_{\text{ex}}^{(2)} > 0$ is related to perpendicular alignment of magnetizations. The exchange stiffness terms for magnetic sublayers are not included in Eq. (1) because they are small for sublayer thicknesses of a few nm as compared to other terms [43]. In the following, the exchange stiffness terms will be neglected in the first approximation and uniform sublayer magnetizations will be assumed for the samples studied.

At equilibrium, the magnetization vectors arranged in non-collinear configuration for the case of mixed BL and BQ interlayer couplings take in symmetrical trilayer the angular positions at angles $\theta_1 = \theta_2 = \theta$ and $\varphi_1 = -\varphi_2 = \varphi$ (see Fig. 1). The dependence of the equilibrium angles θ and φ on the magnitude H and orientation angle θ_H of magnetic field can be determined from numerical minimization of Eq. (1), in general in the $\theta_1, \varphi_1, \theta_2, \varphi_2$ space, and for symmetrical trilayer in the θ, φ space. For special cases of normal ($\theta_H = 0$) and in-plane ($\theta_H = \pi/2$) field directions these angles can be determined analytically, and hence formulas for the perpendicular m_z and parallel-to-plane m_x components of equilibrium sublayer magnetizations a function of the magnetic field magnitude can be derived in both cases. By setting to zero the energy derivatives with respect to the

coordinates θ , φ , a set of two coupled equations for necessary conditions for existence of energy minima were obtained. The equations were next solved with respect to θ and φ , and analytical formulas were derived in the case of (a) in-plane and (b) perpendicular-to-plane hysteresis loops. All the formulas derived were additionally verified in the procedure of global energy numerical minimization. In the following, for the aim of this study, we will be focused on the case of coexisting BL and BQ IEC of magnitudes fulfilling the condition $|H_{\text{ex}}^{(1)}/2H_{\text{ex}}^{(2)}| \leq 1$. We will also consider the most general case when the magnetic field is not coplanar with the magnetization vectors, as it is for the case of easy-plane magnetic anisotropy (see Fig. 1).

For $H = 0$, the sublayer magnetizations remain in the sample easy plane, hence $\theta = \pi/2$, and derived zero-field equilibrium angle φ_0 , the canting angle δ_0 , and the projection of the magnetizations on the x axis m_x^0 are

$$\varphi_0 = 0.5 \arccos\left(\frac{H_{\text{ex}}^{(1)}}{2H_{\text{ex}}^{(2)}}\right), \quad (2a)$$

$$\delta_0 = 2\varphi_0 = \arccos\left(\frac{H_{\text{ex}}^{(1)}}{2H_{\text{ex}}^{(2)}}\right), \quad (2b)$$

$$m_x^0 = \cos(\varphi_0) = \sqrt{\frac{H_{\text{ex}}^{(1)}}{4H_{\text{ex}}^{(2)}} + \frac{1}{2}}. \quad (2c)$$

For $H > 0$, the formulas describing the hysteresis loops depend on the magnetic field orientation.

(a) For the in-plane hysteresis loop, the magnetic field is parallel to the sample easy plane, thus, θ_H and θ angles are equal to $\pi/2$. The equilibrium angle φ , and hence also the canting angle $\delta = 2\varphi$, can be calculated from the equilibrium equation derived by equaling to zero the derivative of Eq. (1) with respect to φ , as $8H_{\text{ex}}^{(2)} \cos(\varphi)^3 - (2H_{\text{ex}}^{(1)} + 4H_{\text{ex}}^{(2)}) \cos(\varphi) - H = 0$. The projection $m_x = \cos(\varphi)$ of the sublayer magnetizations on the x axis as a function of H is then given explicitly by the formula

$$m_x = \cos(\varphi) = h + \frac{2H_{\text{ex}}^{(1)} + 4H_{\text{ex}}^{(2)}}{24H_{\text{ex}}^{(2)}h}, \quad (3)$$

where

$$h = \sqrt[3]{\frac{H}{16H_{\text{ex}}^{(2)}} + \sqrt{\frac{H^2}{256(H_{\text{ex}}^{(2)})^2} - \frac{(2H_{\text{ex}}^{(1)} + 4H_{\text{ex}}^{(2)})^3}{13\,824(H_{\text{ex}}^{(2)})^3}}}.$$

The normalized to unity in-plane hysteresis loop magnitude is described by $m_x(H)$ dependence which achieves remanence m_x^{rem} equal to m_x^0 [see Eq. (2c)]. With increasing H , the angles φ and δ tend to zero, while $m_x = \cos(\varphi)$ saturates to $m_x = 1$ at saturation field $H_{\parallel}^{\text{sat}}$ given by

$$H_{\parallel}^{\text{sat}} = 4H_{\text{ex}}^{(2)} - 2H_{\text{ex}}^{(1)}. \quad (4)$$

(b) For the perpendicular-to-plane hysteresis loop the magnetic field is perpendicular to the sample plane $\theta_H = 0$. The magnetization angles θ and φ depend on H magnitude, and the dependence can be determined analytically by solving the set of equilibrium equations obtained by equaling to zero the derivatives of Eq. (1) with respect to both θ and φ . The

normalized to unity magnitude of perpendicular-to-plane hysteresis loop is described by $m_z = \cos(\theta)$ on H dependence, given by the projection equal to m_z of sublayer magnetizations on the z axis. The $m_z(H)$ function depends on whether the H value is less or greater than the critical field H^{cr} , given by

$$H^{\text{cr}} = -H^{\text{eff}} \sqrt{\frac{H_{\text{ex}}^{(1)}}{4H_{\text{ex}}^{(2)}} + \frac{1}{2}} = -H^{\text{eff}} m_x^0. \quad (5)$$

For $H \leq H^{\text{cr}}$, φ increases from φ_0 to $\pi/2$ and θ decreases from $\pi/2$ to $\theta^{\text{cr}} = \varphi_0$ with H . Within this H -field range, the magnetization curve exhibits linear magnetic field dependence

$$m_z = \cos(\theta) = -\frac{H}{H^{\text{eff}}}, \quad (6)$$

and the magnetization's canting angle remains equal to $\delta_0 = 2\varphi_0$. For $H \geq H^{\text{cr}}$, $\varphi = \pi/2$ and θ decreases from $\theta^{\text{cr}} = \varphi_0$ to 0 with H . The m_z component depends on H nonlinearly, as follows from the solution of equilibrium equation: $8H_{\text{ex}}^{(2)} \cos(\theta)^3 - (H^{\text{eff}} + 2H_{\text{ex}}^{(1)} + 4H_{\text{ex}}^{(2)}) \cos(\theta) - H = 0$, and it is then given explicitly by the formula

$$m_z = \cos(\theta) = \sigma + \frac{H^{\text{eff}} + 2H_{\text{ex}}^{(1)} + 4H_{\text{ex}}^{(2)}}{24H_{\text{ex}}^{(2)}\sigma}, \quad (7)$$

where

$$\sigma = \sqrt[3]{\frac{H}{16H_{\text{ex}}^{(2)}} + \sqrt{\frac{H^2}{256(H_{\text{ex}}^{(2)})^2} - \frac{(H^{\text{eff}} + 2H_{\text{ex}}^{(1)} + 4H_{\text{ex}}^{(2)})^3}{13\,824(H_{\text{ex}}^{(2)})^3}}}.$$

As it follows from Eqs. (5) and (6), m_z takes the value of $m_z^{\text{cr}} = m_x^0$ at $H = H^{\text{cr}}$. The perpendicular-to-plane hysteresis on H dependence, given by $m_z = \cos(\theta)$, achieves saturation value $m_z = 1$ for $\theta = 0$ at saturation field H_{\perp}^{sat} :

$$H_{\perp}^{\text{sat}} = -H^{\text{eff}} + 4H_{\text{ex}}^{(2)} - 2H_{\text{ex}}^{(1)}. \quad (8)$$

Using the values of $H_{\parallel}^{\text{sat}}$, H_{\perp}^{sat} , m_x^{rem} , and/or m_z^{cr} determined from the corresponding experimental hysteresis loops, one can estimate the effective anisotropy H^{eff} and interlayer coupling fields $H_{\text{ex}}^{(1)}$ and $H_{\text{ex}}^{(2)}$ from the formulas

$$H^{\text{eff}} = H_{\parallel}^{\text{sat}} - H_{\perp}^{\text{sat}}, \quad (9a)$$

$$H_{\text{ex}}^{(1)} = \frac{H_{\parallel}^{\text{sat}}(1 - 2m^2)}{4(m^2 - 1)}, \quad (9b)$$

$$H_{\text{ex}}^{(2)} = \frac{H_{\parallel}^{\text{sat}}}{8(1 - m^2)}, \quad (9c)$$

where $m = m_x^{\text{rem}} = m_z^{\text{cr}} = m_x^0$. It should be emphasized that on the basis of the value of the parameter m alone, which can be estimated from experimental hysteresis loops, it is possible to determine the sign of BL IEC. Namely, from Eq. (9b) it follows that there is a limit value $m_l = 1/\sqrt{2} \approx 0.707$, below which BL IEC is antiferromagnetic, and above it is ferromagnetic.

It has been checked that the values of magnetization components m_x , m_z and critical points on the hystereses, calculated from the corresponding analytical formulas with the use of the set of $H_{\text{ex}}^{(1)}$, $H_{\text{ex}}^{(2)}$, and H^{eff} parameters determined in Sec. IV A,

agree to within numerical precision with the ones calculated from numerical minimization of Eq. (1).

B. Magnetization precession dispersion relations

To derive the solutions for the magnetization precession dispersion relations in the case of coexisting BL and BQ IEC we will use the approximation for the set of coupled Landau-Lifshitz-Gilbert equations with damping terms neglected. This approach is justified for the aim of comparison of the mode frequencies with experiment since the damping terms in LLG equations are usually negligibly small as compared to frequency terms. One of the examples of good applicability of the approximation was given for the case of BL IEC in synthetic antiferromagnets in Ref. [24].

The set of coupled equations takes the form

$$\frac{d\mathbf{M}_i}{dt} = -\gamma[\mathbf{M}_i \times \mathbf{H}_i^{\text{eff}}], \quad (10)$$

where \mathbf{M}_i is the magnetization of i th sublayer ($i = 1, 2$), and $\gamma = \frac{g\mu_B}{\hbar}$, where g is the gyromagnetic splitting factor ($g = 2.0023$ for free electron). The magnetization precessions occur due to torques acting on \mathbf{M}_i from the effective fields $\mathbf{H}_i^{\text{eff}} = -(1/M_s)\nabla_i E$, where E is the total energy for the trilayer, which in spherical coordinates is given by Eq. (1). Expressing E in Eq. (1) in the equivalent vectorial form, $\mathbf{H}_i^{\text{eff}}$

can be derived as given by the formula

$$\mathbf{H}_{1(2)}^{\text{eff}} = -\frac{1}{M_s} \frac{\partial E}{\partial \mathbf{m}_{1(2)}} = \mathbf{H} - H^{\text{eff}}\mathbf{z} + H_{\text{ex}}^{(1)}\mathbf{m}_{2(1)} - H_{\text{ex}}^{(2)}\mathbf{m}_{2(1)}(\mathbf{m}_1 \cdot \mathbf{m}_2), \quad (11)$$

where \mathbf{m}_1 and \mathbf{m}_2 are relative magnetization vectors of the sublayers 1 and 2, and \mathbf{z} is the unit vector along the z axis.

In the following, we derive the formulas for symmetrical trilayer for arbitrary direction of external magnetic field in the presence of simultaneous BL and BQ IEC using a general approach given by Zhang *et al.* in Ref. [4]. For description of the precession of magnetizations in the spherical coordinate system, as defined in Sec. III A, one assumes small deviations m_{θ_i} and m_{φ_i} of the magnetizations M_i from its equilibrium positions during the precession. One can obtain a general form of equation of motion in a matrix form, expressed by second derivatives of energy with respect to θ_i and φ_i , as in Ref. [4]. Differentiating the energy in Eq. (1), we obtain the following equation of motion:

$$\begin{pmatrix} \omega' + a & b & d & e \\ c & \omega' - a & f & d \\ -d & e & \omega' - a & b \\ f & -d & c & \omega' + a \end{pmatrix} \begin{pmatrix} m_{\theta_1} \\ m_{\varphi_1} \\ m_{\theta_2} \\ m_{\varphi_2} \end{pmatrix} = 0, \quad (12)$$

where

$$\begin{aligned} a &= H \sin(\varphi) \cot(\theta) \sin(\theta_H) + H_{\text{ex}}^{(1)} \sin(2\varphi) \cos(\theta) + 2H_{\text{ex}}^{(2)} \sin(2\varphi) \cos(\theta) [4 \sin(\varphi)^2 \sin(\theta)^2 - 1], \\ b &= H [\cos(\varphi) \sin(\theta_H) / \sin(\theta)] + H_{\text{ex}}^{(1)} \cos(2\varphi) - 2H_{\text{ex}}^{(2)} [\cos(2\varphi) \cos(\theta)^2 + \cos(4\varphi) \sin(\theta)^2], \\ c &= -H [\cos(\theta) \cos(\theta_H) + \cos(\varphi) \sin(\theta) \sin(\theta_H)] - H^{\text{eff}} \cos(2\theta) + H_{\text{ex}}^{(1)} [2 \sin(\varphi)^2 \sin(\theta)^2 - 1] \\ &\quad + 2H_{\text{ex}}^{(2)} \{ [2 \sin(\varphi)^2 \sin(\theta)^2 - 1]^2 - \sin(\varphi)^4 \sin(2\theta)^2 \}, \\ d &= \sin(2\varphi) \cos(\theta) \{ H_{\text{ex}}^{(1)} + H_{\text{ex}}^{(2)} [8 \sin(\varphi)^2 \sin(\theta)^2 - 2] \}, \\ e &= -H_{\text{ex}}^{(1)} \cos(2\varphi) + 2H_{\text{ex}}^{(2)} [\cos(2\varphi) \cos(\theta)^2 + \cos(4\varphi) \sin(\theta)^2], \\ f &= H_{\text{ex}}^{(1)} [1 - 2 \sin(\varphi)^2 \cos(\theta)^2] - H_{\text{ex}}^{(2)} [4 \sin(\varphi)^4 \sin(2\theta)^2 + 2 \cos(2\varphi)], \end{aligned}$$

and $\omega' = i(\omega/\gamma)$.

Equation (12) can be solved by diagonalization of the matrix and obtaining the corresponding eigenvalues and eigenvectors. Among four magnetization precession frequency solutions for ω , only two are positive. The one corresponds to precession mode in which magnetization vectors precess in phase, and is known as acoustic mode with frequency ω_{ac} . In the second mode, known as optic mode with frequency ω_{op} , the magnetizations precess out of phase. The frequencies of the modes can be obtained in analytical form by the calculation of matrix determinant in Eq. (12), from which the biquadratic equation with respect to (ω/γ) can be derived

$$\left(\frac{\omega}{\gamma}\right)^4 + B\left(\frac{\omega}{\gamma}\right)^2 + C = 0, \quad (13)$$

where

$$B = 2(a^2 - d^2 + bc + ef), \quad C = [(a + d)^2 + (b - e)(c + f)][(a - d)^2 + (b + e)(c - f)].$$

It has been checked that the values of the frequencies obtained from the numerical diagonalization of the matrix in Eq. (12) and from the solutions of Eq. (13) are the same to within the numerical precision.

Analytical formulas for ω_{ac} and ω_{op} solutions given by Eq. (13) greatly simplify for the case of $\theta_H = \pi/2$. Setting in Eqs. (12) and (13) $\theta_H = \pi/2$ and $\theta = \pi/2$, the formulas can be written in compact forms

$$\omega_{\text{ac}} = \gamma \sqrt{-Hm_x [H^{\text{eff}} - Hm_x - 2H_{\text{ex}}^{(1)}(m_x^2 - 1) + 4H_{\text{ex}}^{(2)}(m_x^2 - 1)(2m_x^2 - 1)],} \quad (14a)$$

$$\omega_{\text{op}} = \gamma \sqrt{[Hm_x + 2H_{\text{ex}}^{(1)}(2m_x^2 - 1) - 4H_{\text{ex}}^{(2)}(2(2m_x^2 - 1)^2 - 1)][Hm_x - H^{\text{eff}} + 2H_{\text{ex}}^{(1)}m_x^2 + 4H_{\text{ex}}^{(2)}m_x^2 - 8H_{\text{ex}}^{(2)}m_x^4],} \quad (14b)$$

where m_x is given by Eq. (3).

For $H = 0$, $m_x = m_x^0$ depends, accordingly to Eq. (2c), on relative values of $H_{\text{ex}}^{(1)}$ and $H_{\text{ex}}^{(2)}$ only, and Eqs. (14a) and (14b) further simplify. The frequency of the acoustic mode is equal to zero, and for the optic mode is given by the formula

$$\omega_{\text{op}}^0 = \gamma \sqrt{\frac{H^{\text{eff}}(H_{\text{ex}}^{(1)2} - 4H_{\text{ex}}^{(2)2})}{H_{\text{ex}}^{(2)}}}. \quad (15)$$

From the above formula it follows that for $H = 0$ the optic mode frequency ω_{op}^0 increases with the amplitude of effective anisotropy field H^{eff} (note that for the case of shape anisotropy only, $H^{\text{eff}} = -4\pi M_s < 0$). Since the value of ω_{op}^0 depends on the combination of values of BL and BQ IEC parameters, $H_{\text{ex}}^{(1)}$ and $H_{\text{ex}}^{(2)}$, the optic mode frequency can even reach zero in the case of $|H_{\text{ex}}^{(1)}| \approx 2H_{\text{ex}}^{(2)}$, which will never happen if only bilinear coupling is present in the system, and the biquadratic one is absent.

C. Gilbert damping and spin-pumping damping of magnetization precession

In Sec. III B, we derived analytical formulas for dispersion relations, obtained as solutions of LLG equations without damping in the case of symmetrical trilayer with mixed BL and BQ IEC. To describe the magnetization precession damping observed in FMR and TRMOKE experiments,

various spin-pumping damping terms in addition to Gilbert damping in the case of BL IEC were proposed (see, e.g., [44] and [10,24,45–49]).

In Ref. [50], a nonlocal spin-pumping damping term in the case of BQ IEC and noncollinear magnetizations alignment was proposed and successfully applied to describe the FMR experiment in asymmetric Py/Ru/Pmd trilayers. However, we found this approach less effective for the case of symmetrical trilayer structure corresponding to the Fe/Si MLS studied. Therefore, we adopted the approach of Chiba *et al.* [45] for the case of noncollinear sublayer magnetizations, which has been already successfully applied to describe magnetization precession in TRMOKE experiments in symmetrical SyAF structures with antiferromagnetic IEC [10,49], where noncollinear magnetization alignment arises due to external magnetic field. Moreover, the undertaken approach has additional advantage of accounting the influence of spin-diffusion length parameter, which is an important quantity in the field of spintronics, on spin-pumping damping, what turned out to be important in the case of studied structures.

We modified the coupled LLG equations from Ref. [45] by adding BQ IEC term to the precession part of the equations. The coupled macrospin LLG equations, expressed for Kittel $\mathbf{m} = (\mathbf{m}_1 + \mathbf{m}_2)/2$ and Néel $\mathbf{n} = (\mathbf{m}_1 - \mathbf{m}_2)/2$ vectors [45], with BQ IEC term added are taking the following form:

$$\begin{aligned} \partial_t \mathbf{m} = & -\gamma \mathbf{m} \times \mathbf{H} - \gamma H^{\text{eff}} [(\mathbf{m} \cdot \mathbf{z})\mathbf{m} + (\mathbf{n} \cdot \mathbf{z})\mathbf{n}] \times \mathbf{z} + \alpha_0 (\mathbf{m} \times \partial_t \mathbf{m} + \mathbf{n} \times \partial_t \mathbf{n}) + \alpha_m (\mathbf{m} \times \partial_t \mathbf{m} + \mathbf{n} \times \partial_t \mathbf{n}) \\ & + 2\alpha_m \eta \left[\frac{\mathbf{m} \cdot (\mathbf{n} \times \partial_t \mathbf{n})\mathbf{m}}{1 - \eta(m^2 - n^2)} + \frac{\mathbf{n} \cdot (\mathbf{m} \times \partial_t \mathbf{m})\mathbf{n}}{1 + \eta(m^2 - n^2)} \right], \end{aligned} \quad (16a)$$

$$\begin{aligned} \partial_t \mathbf{n} = & -\gamma \mathbf{n} \times \mathbf{H} - \gamma H^{\text{eff}} [(\mathbf{m} \cdot \mathbf{z})\mathbf{n} + (\mathbf{n} \cdot \mathbf{z})\mathbf{m}] \times \mathbf{z} + \alpha_0 (\mathbf{m} \times \partial_t \mathbf{n} + \mathbf{n} \times \partial_t \mathbf{m}) + \alpha_n (\mathbf{m} \times \partial_t \mathbf{n} + \mathbf{n} \times \partial_t \mathbf{m}) \\ & - 2\alpha_n \eta \left[\frac{\mathbf{m} \cdot (\mathbf{n} \times \partial_t \mathbf{m})\mathbf{m}}{1 + \eta(m^2 - n^2)} + \frac{\mathbf{n} \cdot (\mathbf{m} \times \partial_t \mathbf{n})\mathbf{n}}{1 - \eta(m^2 - n^2)} \right] + 2\gamma [-H_{\text{ex}}^{(1)} + H_{\text{ex}}^{(2)}(m^2 - n^2)] \mathbf{n} \times \mathbf{m}, \end{aligned} \quad (16b)$$

$$\alpha_m = \frac{\alpha_{\text{sp}}}{1 + g_r \coth(d_{\text{NM}}/2\lambda)}, \quad (17a)$$

$$\alpha_n = \frac{\alpha_{\text{sp}}}{1 + g_r \tanh(d_{\text{NM}}/2\lambda)}, \quad (17b)$$

$$\eta = \frac{g_r}{\sinh(d_{\text{NM}}/\lambda) + g_r \cosh(d_{\text{NM}}/\lambda)}, \quad (17c)$$

$$g_r = 2\rho\lambda G_r, \quad (17d)$$

$$\alpha_{\text{sp}} = \gamma \frac{1}{M_s d_{\text{FM}}} \left(\frac{\hbar}{2e} \right)^2 2G_r, \quad (17e)$$

where $\mathbf{H} = (H \sin(\theta_H), 0, H \cos(\theta_H))$, $\mathbf{z} = (0, 0, z)$, $m = |\mathbf{m}|$, $n = |\mathbf{n}|$. In Eq. (16b), in addition to BL IEC which is proportional to $H_{\text{ex}}^{(1)}$ field, we introduced the BQ IEC which relates to $H_{\text{ex}}^{(2)}$ but also depends on values of m and n , as can be derived using Eq. (11). It should be noted that both BL and BQ IEC terms enter only to the second equation for the optic mode, while the term with H^{eff} enter both equations, for the acoustic and optic modes. Both equations are mutually coupled due to various terms including both \mathbf{m} and \mathbf{n} .

In Eqs. (16a) and (16b), α_0 is intrinsic Gilbert damping parameter and coefficients α_m and α_n depend on thickness of nonmagnetic spacer layer d_{NM} and spin-diffusion length λ following Eqs. (17a) and (17b). The α_{sp} is the overall spin-pumping damping parameter, which depends inversely on the ferromagnetic sublayer thickness d_{FM} and its saturation magnetization M_s . The α_{sp} is proportional to the real part of the spin-mixing conductance for the FM/NM interface G_r in Eq. (17e), but does not depend on the resistivity of NM layer ρ , which enter Eq. (17d) for the dimensionless parameter g_r .

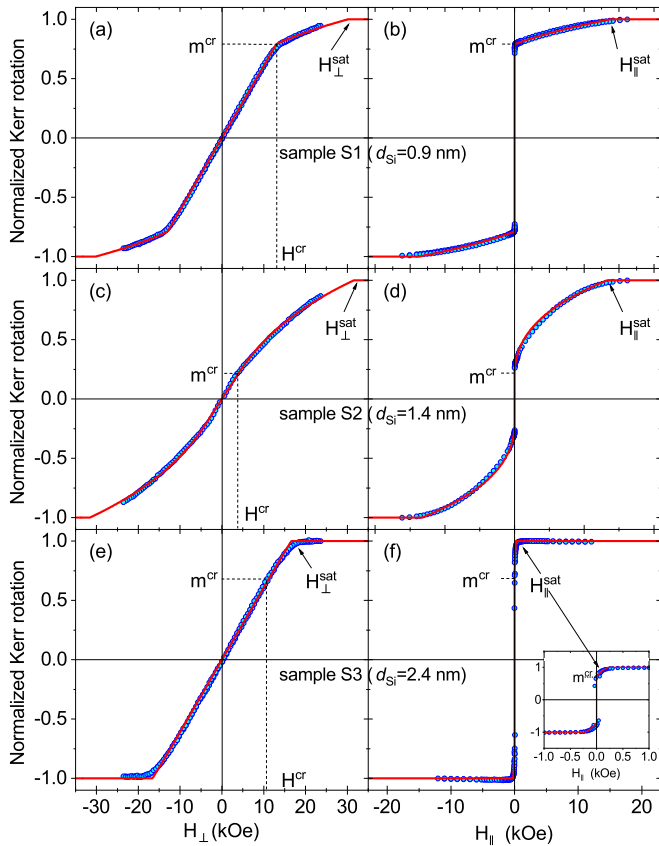


FIG. 2. Normalized hysteresis loops in polar [(a), (c), (e)] and longitudinal [(b), (d), (f)] magneto-optical Kerr effect in Fe/Si(d_{Si}) multilayers for sample S1 ($d_{\text{Si}} = 0.9$ nm) [(a), (b)], S2 ($d_{\text{Si}} = 1.4$ nm) [(c), (d)], and S3 ($d_{\text{Si}} = 2.4$ nm) [(e), (f)]. The experimental data are marked by circles and theoretical ones by red solid lines. Characteristic hysteresis points m^{cr} , H_{\perp}^{sat} , $H_{\parallel}^{\text{sat}}$, and H^{cr} (see text) are indicated by dashed lines and arrows.

Note that the backflow efficiency of the spin current η tends to unity, a_m to zero, and a_n to α_{sp} for increasing values of λ in Eqs. (17a)–(17c).

We solved the above LLG equations numerically with inclusion of all damping terms for the general case of coexisting BL and BQ IEC and for *arbitrary* direction of magnetic field (tuning the α_{sp} , g_r , and λ parameters) in the procedure of fitting the LLG solutions to the experimental TRMOKE traces in Sec. IV C.

IV. EXPERIMENTAL RESULTS: COMPARISON WITH THEORY AND DISCUSSION

A. Static polar and longitudinal magneto-optical Kerr effect hysteresis loops

The hysteresis loops measured in polar and longitudinal MOKE geometry in the [Fe/Si(d_{Si})]₁₅ multilayers are shown in Fig. 2 together with the corresponding theoretical curves obtained as a result of fitting procedure performed. The polar hystereses shown in Figs. 2(a), 2(c), and 2(e) correspond to magnetizations reversal from the in-plane to the magnetic field direction, applied perpendicularly to the sample plane. For all samples the reversal process occurs within two magnetic

field ranges. In the first range m_z component exhibits linear increase with H field up to H^{cr} , and nonlinear one in the second range from H^{cr} up to H_{\perp}^{sat} . The longitudinal hystereses shown in Figs. 2(b), 2(d), and 2(f) describe the magnetization processes in which the sublayer magnetizations rotate within the sample plane along the H -field direction. The magnetization component m_x increases from $m^{\text{cr}} = m_x^0$ value at zero field to saturation at $H_{\parallel}^{\text{sat}}$, with the accompanying decreasing canting angle from its initial value δ_0 to zero.

In order to roughly estimate the effective fields $H_{\text{ex}}^{(1)}$ and $H_{\text{ex}}^{(2)}$ corresponding to BL and BQ IEC, it is sufficient to use formulas given by Eqs. (9b) and (9c), with m^{cr} and $H_{\parallel}^{\text{sat}}$ only determined from longitudinal hysteresis loops. The sign of BL IEC can be determined from magnetization curves in Figs. 2(b), 2(d), and 2(f) using the values of m^{cr} , which are equal to ≈ 0.8 , ≈ 0.25 , and ≈ 0.65 for samples S1, S2, and S3, respectively. Comparing these values with the $m_l \approx 0.707$ limit value, discussed in Sec. III A, it can be inferred that BL IEC is ferromagnetic for sample S1, and antiferromagnetic for samples S2 and S3, respectively. With the use of $H_{\parallel}^{\text{sat}}$ values determined for corresponding samples [see Figs. 2(b), 2(d), and 2(f)], approximate $H_{\text{ex}}^{(1)}$ and $H_{\text{ex}}^{(2)}$ parameter values can be then obtained. On the other hand, to obtain approximate H^{eff} parameter values, well-determined saturation fields H_{\perp}^{sat} in polar hysteresis loops are additionally required, as it follows from Eq. (9a). However, as it can be seen in Figs. 2(a) and 2(c), the polar hystereses apparently do not achieve saturation within the available magnetic field range. Therefore, to obtain reliable values of all IEC parameters, the fitting procedure has been applied taking into account also possible lack of saturation. For this aim, it has been allowed that theoretical curves can saturate at higher H_{\perp}^{sat} fields than experimentally available. The theoretical dependencies were fitted, for each sample, to the measured longitudinal and polar Kerr rotation hysteresis loops simultaneously, using Eqs. (3) and (7) with $H_{\text{ex}}^{(1)}$, $H_{\text{ex}}^{(2)}$, and H^{eff} treated as fitting parameters. The best fitted theoretical curves were then extrapolated to the magnetic field of ≈ 35 kOe and normalized to unity together with the corresponding experimental ones. The best fitted $H_{\text{ex}}^{(1)}$, $H_{\text{ex}}^{(2)}$, and H^{eff} parameters were obtained in the fitting procedure, performed independently for all quarters of the hysteresis loops. The mean values of the parameters, together with error bars estimated, are shown in Table I. The theoretical dependencies exhibit excellent agreement with the experiment. Characteristic hysteresis points, i.e., m^{cr} , H_{\perp}^{sat} , $H_{\parallel}^{\text{sat}}$, and H^{cr} , calculated according to Eqs. (2c), (4), (8), and (5) using the determined values of $H_{\text{ex}}^{(1)}$, $H_{\text{ex}}^{(2)}$, and H^{eff} shown in Table I, are indicated in Fig. 2 by dashed lines and arrows. As it is seen from Fig. 2, all the point values are well reproduced by the theory. For example, the critical field H^{cr} , observed in experimental curve for sample S1 in Fig. 2(a), coincides well with the value 12.9 kOe predicted by the theory. For samples S1 and S2, large values of H_{\perp}^{sat} saturation fields 29.5 and 31.4 kOe, respectively, are predicted, which exceed about twice the effective anisotropy fields (see Table I). However, this is not an inconsistency of the model since large values of H_{\perp}^{sat} result from large values of $H_{\text{ex}}^{(1)}$ and $H_{\text{ex}}^{(2)}$ parameters, which contribute additively to H_{\perp}^{sat} according to Eq. (8). Similarly, large values of $H_{\parallel}^{\text{sat}}$ equal to 13.2 and 13.8 kOe, respectively, for these samples are due to a dominant contribution of $H_{\text{ex}}^{(2)}$ to

TABLE I. Bilinear and biquadratic interlayer exchange-coupling fields $H_{\text{ex}}^{(1)}$ and $H_{\text{ex}}^{(2)}$ with corresponding J_1 and J_2 parameters of coupling strengths and the effective magnetic anisotropy field H^{eff} in Fe/Si(d_{Si}) multilayer samples, determined from MOKE hysteresis loops.

Sample	d_{Si} (nm)	$H_{\text{ex}}^{(1)}$ (kOe)	J_1 (mJ/m ²)	$H_{\text{ex}}^{(2)}$ (kOe)	J_2 (mJ/m ²)	H^{eff} (kOe)
S1	0.9	2.3 ± 0.4	0.9 ± 0.2	4.5 ± 0.2	1.8 ± 0.1	-16.3 ± 0.4
S2	1.4	-3.2 ± 0.1	-1.3 ± 0.1	1.8 ± 0.1	0.7 ± 0.1	-17.6 ± 0.9
S3	2.4	-0.010 ± 0.010	-0.005 ± 0.005	0.050 ± 0.010	0.020 ± 0.005	-16.3 ± 0.3

$H_{\parallel}^{\text{sat}}$, as it follows from Eq. (4). In contrast, small value of $H_{\parallel}^{\text{sat}}$ of about 0.2 kOe for sample S3, seen in the inset in Fig. 2(f), results from low values of $H_{\text{ex}}^{(1)}$ and $H_{\text{ex}}^{(2)}$, which cause that H_{\perp}^{sat} is close to H^{eff} for this sample.

The fitted effective magnetic anisotropy field H^{eff} parameters change from -16.3 ± 0.4 to -17.6 ± 0.9 kOe for the samples. These values are in good agreement with the magnetization value $4\pi M_s = 16.7 \pm 0.7$ kOe, extracted from the spontaneous Hall effect measurements for Fe(3 nm)/Si(1.1 nm) multilayers, prepared by the same technique, in Ref. [51]. The coincidence of the H^{eff} and $4\pi M_s$ values indicates that contribution to H^{eff} related to uniaxial anisotropy field $2K_u/M_s$ is within the error bars and can be neglected. Therefore, in the following, for Fe sublayers the value of saturation magnetization $4\pi M_s \approx 16.7 \pm 0.7$ kOe will be assumed for the samples studied.

In Table I, the J_1 and J_2 parameters, which are quantities characterizing coupling strengths independently of magnetic layer thickness, were calculated from the relation $J_i = H_{\text{ex}}^{(i)} M_s d_{\text{Fe}}$ ($i = 1, 2$), using $d_{\text{Fe}} = 3$ nm and saturation magnetization of Fe sublayers assumed above, are presented together with their error bars. As it is seen from Table I, there is a strong BQ of $J_2 = 1.8$ mJ/m², and coexisting weaker BL IEC of $J_1 = 0.9$ mJ/m² in sample S1 with thinnest Si layer. From the ratio of J_1 and J_2 values, the canting angle equal to $\delta_0 = 75 \pm 5^\circ$ is calculated from Eq. (2b), which value is in line with the ferromagnetic type of BL IEC. With increasing Si thickness in sample S2, the ferromagnetic BL IEC changes to strong antiferromagnetic one, with $J_1 = -1.3$ mJ/m² and $J_2 = 0.7$ mJ/m² as compared to sample S1. This change to antiferromagnetic coupling is accompanied by increase of δ_0 well above 90° , to $155^\circ \pm 10^\circ$. For sample S3, where d_{Si} value increases by $\approx 70\%$ as compared to S2, both BL and BQ IEC are very weak, with J_1 and J_2 being reduced by one to two orders of magnitude. However, the antiferromagnetic character of BL IEC, and nonzero BQ IEC remain still for sample S3. The weak antiferromagnetic BL IEC is accompanied by canting angle of value $95^\circ \pm 10^\circ$, being only slightly greater than 90° , which is the exact δ_0 value for BQ IEC alone.

B. Magnetization precession and dispersion relations

1. Transient Kerr rotation

The changes of the $\mathbf{M}(t)$ vs delay time t between pump and probe pulses are detected in reflection geometry as transient Kerr rotation $\Delta\theta_K(t)$ in TRMOKE experiment. Because of the presence of interlayer coupling determined from the measured static hysteresis loops, as was discussed in Sec. IV A, two magnetization precession modes in all the samples are expected. Therefore, it is convenient to express the measured TRMOKE signals as a sum of the components given by the

formula

$$\Delta\theta_K(t) = A_1 \exp\left(-\frac{t}{\tau_1}\right) \sin(2\pi f_1 t + \varphi_1) + A_2 \exp\left(-\frac{t}{\tau_2}\right) \sin(2\pi f_2 t + \varphi_2) + B(t), \quad (18)$$

where A_i , f_i , φ_i , and τ_i are the amplitude, frequency, phase, and relaxation time of the i th ($i = 1, 2$) magnetization precession component in the TRMOKE signal, respectively. The first two terms in Eq. (18), denoted hereafter as $\Delta\theta_K^{\text{osc}}(t)$, represent damped oscillatory functions describing decaying of magnetization precession, and $B(t)$ represents a slowly varying nonoscillating background, related to sample demagnetization and recovery processes.

For all measured $\Delta\theta_K(t)$ dependencies, the fitting procedure using Eq. (18) with $B(t)$ given by biexponential backgrounds, was performed. The $\Delta\theta_K^{\text{osc}}(t)$ terms have been determined by subtracting fitted $B(t)$ background terms from the measured $\Delta\theta_K(t)$. The procedure was applied to all experimental data, and the oscillatory $\Delta\theta_K^{\text{osc}}(t)$ dependencies have been extracted and are shown in Figs. 3(a), 3(c), and 3(e) for samples S1, S2, and S3, respectively. In the experimental $\Delta\theta_K^{\text{osc}}(t)$ traces, two oscillatory components of different frequencies are seen. The corresponding precession modes will be considered further quantitatively as the acoustic and optic modes characterized by the lower and higher frequencies, denoted as ω_{ac} and ω_{op} , respectively. The fitted theoretical $\Delta\theta_K^{\text{osc}}(t)$ dependencies are in very good agreement with the experimental ones, and both are plotted in Figs. 3(a), 3(c), and 3(e) for increasing magnetic field H magnitudes up to 6.5 kOe, indicated on vertical axes, and orientation angles $\theta_H = 10^\circ$, 25° , and 50° . As it is seen, the $\Delta\theta_K^{\text{osc}}(t)$ dependencies significantly differ between the samples and strongly change with H and θ_H .

For better visualization of the precession mode evolution, fast Fourier transforms (FFT) of the fitted $\Delta\theta_K^{\text{osc}}(t)$ dependencies were calculated, and the results are shown in Figs. 3(b), 3(d), and 3(f) for samples S1, S2, and S3, respectively. Occurrence of two precession modes, of frequencies ω_{ac} and ω_{op} determined by peak positions in FFT spectra marked with vertical dashed lines in Figs. 3(b), 3(d), and 3(f), can be observed. It is seen that ω_{ac} frequencies change in a different way with H field and θ_H angle than ω_{op} ones, and the evolutions differ also between the samples. A similar diversity also exists for the peak amplitudes of the modes. Since the amplitudes of a part of the peaks are very small as compared to others, and peaks are overlapped, these mode frequencies are hardly determinable. Therefore, the FFT spectra were taken only as a qualitative illustration of the mode evolution in the samples studied. For the most reliable, quantitative

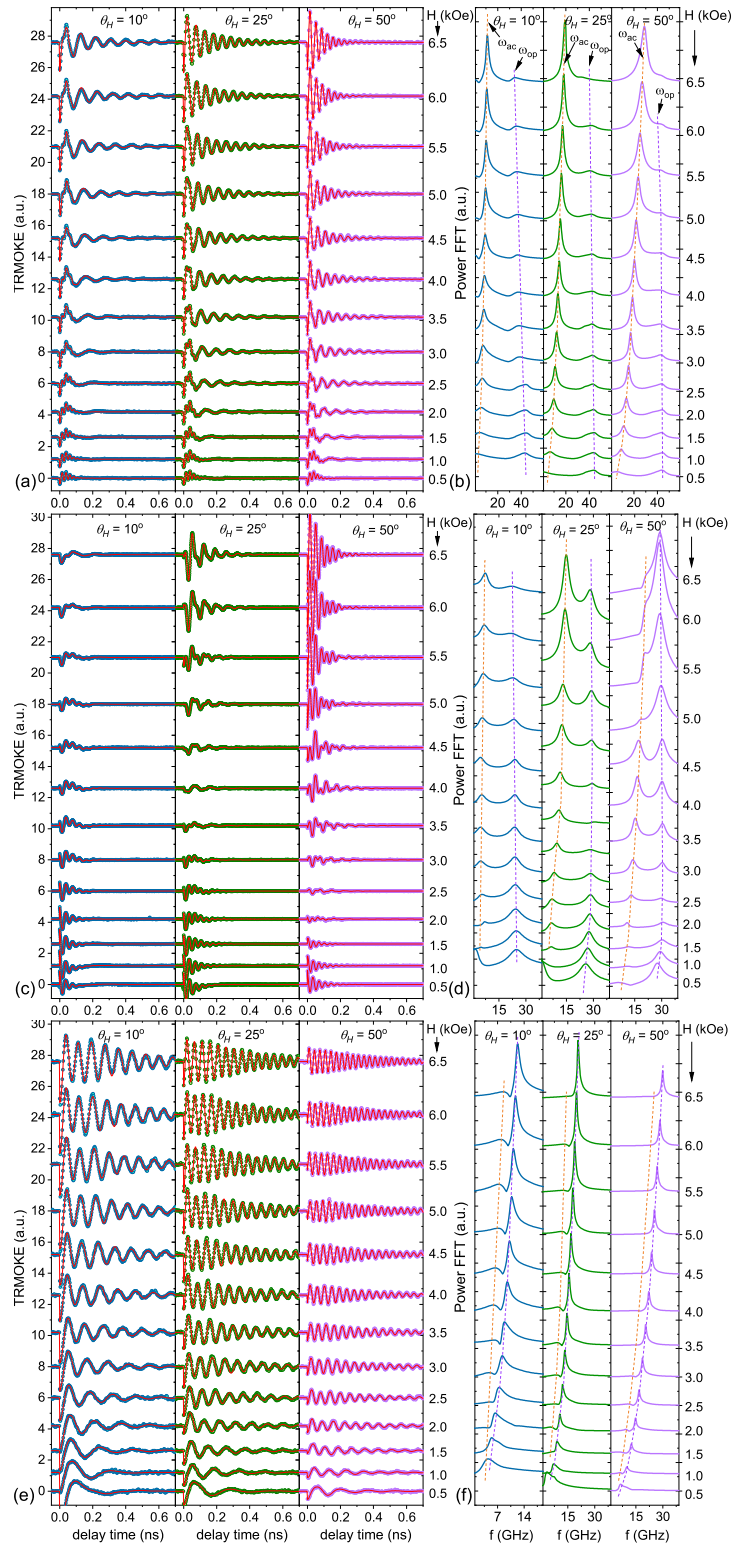


FIG. 3. Transient Kerr rotation signals and their FFT transforms as a function of magnetic field magnitude H and orientation angle θ_H in Fe/Si(d_{Si}) multilayers for sample S1 ($d_{\text{Si}} = 0.9$ nm) [(a), (b)], S2 ($d_{\text{Si}} = 1.4$ nm) [(c), (d)], and S3 ($d_{\text{Si}} = 2.4$ nm) [(e), (f)]. In (a), (c), and (f) are plotted experimental (circles) and fitted (solid lines) $\Delta\theta_{\text{K}}^{\text{osc}}$ vs delay-time t dependencies, and in (b), (d), and (f) FFT transforms of the fitted ones (see text). The curves are marked by magnetic field values and shifted in vertical scales for clarity. The dashed vertical lines in (b), (d), and (f) indicate approximate peak positions of acoustic and optic precession modes in the FFT spectra.

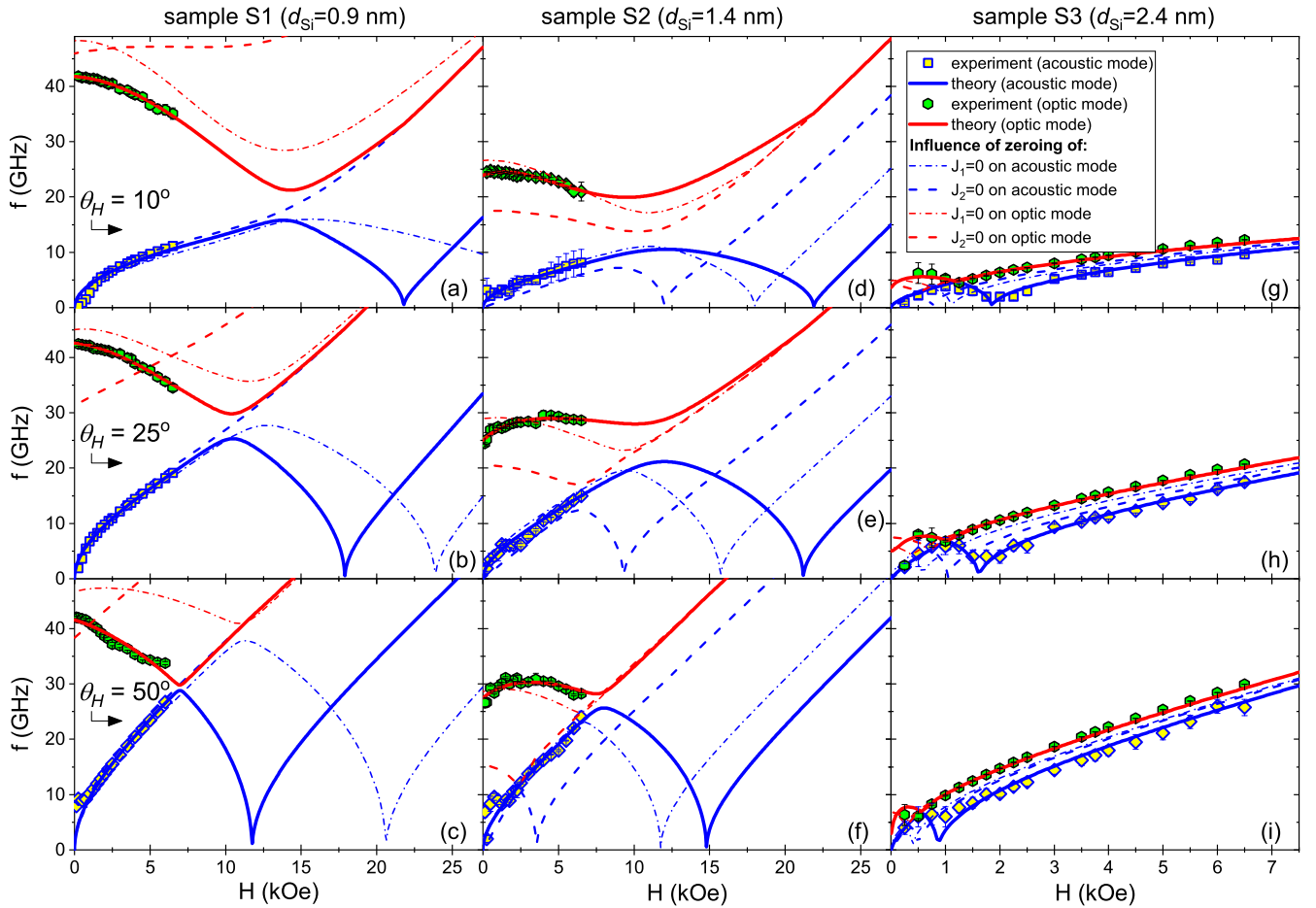


FIG. 4. Magnetization precession frequency dependencies on magnetic field H (symbols), best fitted to experimental TRMOKE signals with the use of Eq. (18) in Fe/Si(d_{Si}) multilayers for samples S1 [(a)–(c)], S2 [(d)–(f)], and S3 [(g)–(i)] for magnetic field angle θ_H equal to 10° [(a), (d), (f)], 25° [(b), (e), (h)], and 50° [(c), (f), (i)]. The theoretical dispersion curves, best fitted to the data using Eq. (13), are shown for acoustic and optic modes with thick blue and red lines, respectively. For each case, the curves calculated for best fitted parameters except for parameter J_1 set to 0 are shown as thin dashed-dotted lines, and for J_2 set to 0 are shown as thick dashed lines [see the legend in (g)]. Note that vertical frequency axes are scaled according to relation $f = \omega/(2\pi)$.

determination of the mode frequencies, the complete fitting procedure has been performed and the results are described in the next section.

2. Dispersion relations

As a result of the fitting procedure, applied to all the $\Delta\theta_{\text{K}}^{\text{osc}}(t)$ delay-time traces with the use of Eq. (18), the $\omega_{\text{ac}}(H)$ and $\omega_{\text{op}}(H)$ field dependencies were determined, and are shown in Figs. 4(a)–4(i) by symbols for different θ_H angles. As it can be seen in Figs. 4(a)–4(f), characteristic features of experimental $\omega_{\text{ac}}(H)$ and $\omega_{\text{op}}(H)$ dependencies for samples S1 and S2 are as follows: (i) $\omega_{\text{ac}}(H)$ monotonically increase vs H for all θ_H angles within the range of available experimental magnetic field, (ii) $\omega_{\text{op}}(H)$ changes within higher-frequency values and decreases monotonically with H for sample S1, while for S2 the $\omega_{\text{op}}(H)$ exhibits more complex character dependent on θ_H angle, (iii) the separation between optic and acoustic branches decreases as θ_H increases. For sample S3, similar behavior as in S1 and S2 is observed already at low H fields. However, for higher fields, a mode-crossing effect occurs with the crossing field values $H_{\theta_H}^{\text{cross}}$ decreasing

from ≈ 1 kOe to ≈ 0.5 kOe as θ_H increases from 10° to 50° . The acoustic mode exhibits low-value dips, at fields $H_{\theta_H}^{\text{dip}}$ roughly twice of $H_{\theta_H}^{\text{cross}}$ values, followed by further monotonic frequency increase. Qualitatively similar behavior was also observed for various layered structures with BL IEC only, in FMR [4,24,52–55] and TRMOKE [5,7] experiments. It is to be noted that for samples S1 and S2, the mode crossing is clearly visible in experimental data only for $\theta_H = 50^\circ$ at $H \approx 6.5$ kOe.

To explain all the observed $\omega_{\text{ac,op}}(H)$ behavior's diversity on equal foots, the fitting procedure with the use of theoretical dispersion relations, calculated from solutions of Eq. (13), was performed. For a given sample, the fitting procedure was applied within the entire H -field range for each θ_H angle, 10° , 25° , and 50° , for both $\omega_{\text{ac}}(H)$ and $\omega_{\text{op}}(H)$ dependencies simultaneously. As a result, the sets of $H_{\text{ex}}^{(1)}$, $H_{\text{ex}}^{(2)}$, and H^{eff} parameters were obtained for each θ_H angle independently. The dimensionless gyromagnetic g -factor values were fitted simultaneously in each case. Since the parameter values fitted for different θ_H angles appeared to have some spread, the mean values with corresponding error bars have been calculated and are presented in Table II.

TABLE II. Bilinear and biquadratic interlayer exchange-coupling fields $H_{\text{ex}}^{(1)}$ and $H_{\text{ex}}^{(2)}$ with corresponding J_1 and J_2 parameters of coupling strengths and the effective magnetic anisotropy field H^{eff} in Fe/Si(d_{Si}) multilayer samples, determined from TRMOKE experiment. The g is the dimensionless gyromagnetic splitting factor.

Sample	d_{Si} (nm)	$H_{\text{ex}}^{(1)}$ (kOe)	J_1 (mJ/m ²)	$H_{\text{ex}}^{(2)}$ (kOe)	J_2 (mJ/m ²)	H^{eff} (kOe)	g
S1	0.9	4.0 ± 1.5	1.6 ± 0.6	4.5 ± 0.7	1.8 ± 0.3	-13.3 ± 3.3	2.16 ± 0.26
S2	1.4	-2.1 ± 1.6	-0.9 ± 0.7	2.4 ± 0.6	1.0 ± 0.3	-10.2 ± 1.9	2.08 ± 0.16
S3	2.4	-0.115 ± 0.095	-0.045 ± 0.040	0.080 ± 0.020	0.035 ± 0.010	-13.7 ± 1.5	2.14 ± 0.16

The coupling strengths J_i , calculated from corresponding $H_{\text{ex}}^{(i)}$ parameters in a similar way as in Sec. IV A, together with estimated error bars, are listed in Table II. In sample S1, BL IEC is ferromagnetic with $J_1 = 1.6$ mJ/m², and in S2, it is antiferromagnetic with $J_1 = -0.9$ mJ/m². Even though BL IEC in sample S1 prefers parallel alignment, strong BQ IEC with $J_2 = 1.8$ mJ/m² enforces canting arrangement of the Fe sublayer magnetization vectors. On the other hand, the strong antiferromagnetic BL IEC in sample S2, preferring antiparallel alignment, is influenced by a strong BQ IEC with $J_2 = 1.0$ mJ/m², leading also to noncollinear magnetization arrangement. As a result, the zero-field canting angles δ_0 , which depend on the determined values of $H_{\text{ex}}^{(1)}$ and $H_{\text{ex}}^{(2)}$ parameters, accordingly to Eq. (2b), differ in both samples, having values of $\sim 65 \pm 5^\circ$ and $\sim 120 \pm 20^\circ$ for samples S1 and S2, respectively.

In the case of sample S3, significant antiferromagnetic BL IEC reduction, from one to two orders of magnitude, is observed. As Si thickness is changing from $d_{\text{Si}} = 1.4$ to $d_{\text{Si}} = 2.4$ nm, the reduction of coupling strengths with the increase of Si thickness is described by exponential decay relation $J_i \sim \exp(-d_{\text{Si}}/\lambda_i)$, with the decay lengths λ_i estimated in the range of 0.2–0.4 nm. The decay lengths are of the same order of magnitude as reported for different Fe/Si structures [32] and explained within the framework of Slonczewski's loose spin model [56].

The results obtained so far allow to compare quantitatively the $H_{\text{ex}}^{(i)}$ and H^{eff} parameter values determined from dynamic TRMOKE experiment (shown in Table II) with the ones obtained from measurements of static MOKE hysteresis loops (shown in Table I). As it is seen, the parameter values determined in both experiments agree to within error bars estimated. The only exception is H^{eff} parameter which values are in average considerably smaller in Table II as compared to Table I. The reasons for the differences are not fully identified as yet. One of the possible reasons is that H^{eff} can manifest differently in MOKE and TRMOKE experiments. In particular, in dynamic TRMOKE experiment the magnetization precession is triggered by laser pump pulses which energy can increase the sample temperature. As a result, this may lead to a reduction of H^{eff} values, similarly as reported in Ref. [36]. For Fe/Si multilayers, with sublayer's thicknesses similar as this study, the Curie temperatures reported in the literature are much lower than T_C of pure Fe film [57]. This is related to the fact that Fe readily reacts with Si, forming a rich variety of silicides at the interfaces [32,34]. However, the study of the TRMOKE effects as a function the laser pulse fluence, in order to clarify this possibility, is beyond the scope of this paper.

For analysis of the TRMOKE experimental data, an additional fitting parameter g factor has been determined. For the samples studied, obtained g -factor values were estimated in the range of 2.08–2.16 (see Table II). The mean values of g factor have a tendency to be larger than for thin Fe film, for which we have determined value of $g \approx 2.04$.

The best fitted theoretical $\omega_{\text{ac,op}}(H)$ dependencies are presented in Figs. 4(a)–4(i) with blue and red solid curves for acoustic and optic mode, respectively. As it is seen, the theory reproduces very well the experimental data for both modes and all θ_H angles within error bars for entire H -field range available in the experiment. The $\omega_{\text{ac,op}}(H)$ dependencies, predicted by the theory in H -field range up to ~ 27 kOe, resemble the overall behavior of acoustic and optic modes with presence of BL IEC only, as reported in the literature [4,7,24,52–55]. However, the BQ IEC occurrence significantly affects the $\omega_{\text{ac,op}}(H)$ functions. For example, this is the case of the optical mode frequencies ω_{op}^0 extrapolated to zero field, which can be either determined from fitting procedure, according to Eq. (13), or from analytical expression given by Eq. (15), and which both are in a good agreement with the experimental ω_{op} dependencies extrapolated to zero field. As can be seen from Eq. (15), ω_{op}^0 depends on $H_{\text{ex}}^{(2)}$ even stronger than on $H_{\text{ex}}^{(1)}$ parameter. The decrease of $\omega_{\text{op}}(H)$ as H tends to zero, not reported in the literature but observed in sample S2 for θ_H equal to 25° and 50° and for all θ_H angles in sample S3, results from the same order of $H_{\text{ex}}^{(1)}$ and $H_{\text{ex}}^{(2)}$ values, i.e., when a compensation between BL and BQ IEC occurs, as follows directly from Eq. (15).

The most characteristic feature in the theoretical $\omega_{\text{ac,op}}(H)$ functions is the mode-crossing effect occurring for all cases, with corresponding frequency gaps (also termed in literature as “anticrossing gaps”) between acoustic and optic branches at higher H fields. In the vicinity of the crossing field, acoustic and optic mode hybridization effect, i.e., the magnon-magnon coupling, appears [24,52,58,59]. There is also monotonic evolution of $H_{\theta_H}^{\text{cross}}$ towards higher field values, with simultaneous increase of the frequency gaps as θ_H angle decreases from $\theta_H = 50^\circ$ to 10° [see Figs. 4(a)–4(c) for sample S1, Figs. 4(d)–4(f) for S2, and Figs. 4(g)–4(i) for S3]. Similar θ_H -angle-dependent behavior was also experimentally observed and theoretically explained in synthetic antiferromagnets with BL IEC only [24]. In the present case, it is seen that the mode-crossing field and frequency gap behave differently for coexisting BL and BQ IEC of similar strengths but opposite signs, i.e., for ferromagnetic BL IEC in sample S1 [see Figs. 4(a)–4(c)] and antiferromagnetic BL IEC in S2 [see Figs. 4(d)–4(f)]. In the case of sample S3, similar trend of $H_{\theta_H}^{\text{cross}}$ increase as θ_H decreases is seen, but with $H_{\theta_H}^{\text{cross}}$ values

shifted towards much lower fields as compared to samples S1 and S2.

As the magnetic field increases, the zero-field canting angles δ_0 decrease and further collapse to zero at the field values $H_{\theta_H}^{\text{dip}}$, which depend on θ_H angle, H^{eff} , and IEC parameters for a given sample. The $H_{\theta_H}^{\text{dip}}$ values differ from the saturation fields H_{\perp}^{sat} and $H_{\parallel}^{\text{sat}}$, which were determined in Sec. III A for $\theta_H = 0^\circ$ and 90° . The $H_{\theta_H}^{\text{dip}}$ fields decrease for larger θ_H angle and approach $H_{\parallel}^{\text{sat}}$ at $\theta_H \rightarrow 90^\circ$. Low BL and BQ IEC values in sample S3 cause that dips observed in acoustic frequency modes have a full correspondence in the theory within entire measured field range. In particular, the theory adequately reproduces the experimental frequency data within its error bars for high H fields as well.

We performed additional test calculations to investigate the influence of BL and BQ IEC separately on dispersion relations. For this purpose, calculations of theoretical $\omega_{\text{ac,op}}(H)$ dependencies in a wide H -field range were performed with best fitted parameters values assumed, except of either J_1 or J_2 parameter fixed to zero. The obtained theoretical curves are shown by thin dashed-dotted and dashed curves, respectively, in Fig. 4. As can be seen, for all studied samples, zeroing of the BL IEC, by setting $J_1 = 0$, has little effect on acoustic mode within experimentally available magnetic fields, although considerable differences can be seen for higher H fields. Simultaneously, the optic mode is significantly affected, particularly for sample S1 [see Figs. 4(a)–4(c)]. For higher H fields, the values of $H_{\theta_H}^{\text{cross}}$ and $H_{\theta_H}^{\text{dip}}$ increase for sample S1 with ferromagnetic BL, and decrease for samples S2 and S3 with antiferromagnetic BL IEC, for each θ_H angle in comparison to exact solution. Much more significant deviations appear in the case of zeroing of the BQ IEC, i.e., by setting $J_2 = 0$, in both acoustic and optic branches. Strong reduction of $H_{\theta_H}^{\text{cross}}$ and $H_{\theta_H}^{\text{dip}}$ values, dependent on θ_H , is seen for sample S2 [see Figs. 4(d)–4(f)], while for S1 no mode-crossing effect can be observed at all. This result can be expected in advance in the case of ferromagnetic coupling between the layers. In conclusion, BQ IEC, coexisting with antiferromagnetic BL IEC, is equally important for reliable description of the dispersion relations.

C. Damping of magnetization precession

1. Effective damping parameters

Along with dispersion relations discussed in Sec. IV B 2, relaxation times τ_{ac} and τ_{op} of corresponding acoustic and optic modes, respectively, were simultaneously determined in the fitting procedure of $\Delta\theta_{\text{K}}^{\text{osc}}(t)$ dependencies using Eq. (18). These parameters were next used in determination of the effective damping of each frequency mode, accordingly to relation $\alpha_{\text{ac(op)}}^{\text{eff}} = 1/(\omega_{\text{ac(op)}}\tau_{\text{ac(op)}})$.

The $\alpha_{\text{ac,op}}^{\text{eff}}(H)$ dependencies for different θ_H angles are shown in Fig. 5. Strong changes of effective damping parameters with θ_H angles, similarly as reported in Refs. [60,61], can be noticed. For sample S1, $\alpha_{\text{ac}}^{\text{eff}}$ at low H fields is several times larger than $\alpha_{\text{op}}^{\text{eff}}$, which is caused by decreasing of $\omega_{\text{ac}}(H)$ as H approaches zero. The magnitude of $\alpha_{\text{ac}}^{\text{eff}}(H)$ dependencies decreases, while $\alpha_{\text{op}}^{\text{eff}}(H)$ weakly changes as θ_H is increasing.

For all θ_H angles, $\alpha_{\text{ac}}^{\text{eff}}$ decreases several times with H , while about twofold increase of $\alpha_{\text{op}}^{\text{eff}}$ is observed. Similar behavior can be seen in sample S2 for $\alpha_{\text{ac}}^{\text{eff}}$. Different behavior, as compared to samples S1 and S2, can be seen for sample S3. The $\alpha_{\text{op}}^{\text{eff}}$ decreases strongly with field, achieving smallest values at higher fields among all samples. The $\alpha_{\text{ac}}^{\text{eff}}(H)$ dependencies exhibit maxima at H -field values corresponding to $\omega_{\text{ac}}^{\text{eff}}(H)$ dips at $H_{\theta_H}^{\text{dip}}$ fields, discussed in Sec. IV B 2 [see Figs. 4(g)–4(i)]. The last behavior can be explained through inverse proportionality relation of $\alpha_{\text{ac}}^{\text{eff}}(H)$ with respect to $\omega_{\text{ac}}^{\text{eff}}(H)$, exhibiting minima at the dips. For magnetic fields exceeding $H_{\theta_H}^{\text{dip}}$ values, $\alpha_{\text{ac}}^{\text{eff}}(H)$ decreases, being several times larger than $\alpha_{\text{op}}^{\text{eff}}(H)$.

2. Gilbert damping and spin-pumping-damping-related model parameters

In order to study the behavior of intrinsic damping parameters, i.e., Gilbert damping α_0 and spin-pumping damping α_{sp} parameters in the presence of interlayer exchange coupling, numerical solving of coupled equations (16a) and (16b) was carried out with simultaneous fitting to experimental TRMOKE traces shown in Fig. 3. In addition to α_0 and α_{sp} , the λ and g_r were taken as a fitting parameters in the damping model used. To avoid possible correlations between model parameters, their values were kept constant over the entire H -field range. This procedure was performed for each azimuth and mean values of the parameters with their standard deviations were estimated for each sample. In the fitting procedure, the $H_{\text{ex}}^{(1)}$, $H_{\text{ex}}^{(2)}$, and H^{eff} parameters were allowed to be changed within bounds specified by the parameter's uncertainties estimated in Table II. The best fitted values of α_0 , α_{sp} , and λ parameters together with error bars estimated are shown in Table III. The estimated g_r parameter values remain within 10 ± 3 range for all samples. From the obtained α_{sp} parameter values, the real parts of the spin-mixing conductance for the FM/NM interface G_r parameter values for each sample were determined using Eq. (17e) and are shown in Table III. In this estimation, we used the value of magnetic Fe sublayer thickness $d_{\text{Fe}} = 3$ nm and the values of magnetization M_s determined from H^{eff} values together with error bars listed in Table II.

Analyzing the intrinsic damping parameters some general observations can be noticed:

(i) The intrinsic Gilbert damping parameter α_0 for sample S3 has a value of the same order as reported for trilayer structures consisting of magnetic sublayers of iron-containing alloys. For example, in CoFeB/Ru/CoFeB trilayers α_0 was estimated from TRMOKE experiment to 0.011 in Ref. [49], and in Co-Fe/Ru/Co-Fe trilayers to ≈ 0.01 , approximated from high H -field α_{eff} values [62]. The values of damping parameter α_0 for samples S1 and S2 are noticeably larger remaining in the range of 0.06–0.08 as compared to S3, and it can be probably ascribed to higher magnetic inhomogeneity of the Fe/Si interface region microstructure, which relative volume decreases with nominal d_{Si} thickness.

(ii) The spin-pumping damping parameter α_{sp} has the largest value of ≈ 0.088 for sample S1 which decreases to ≈ 0.067 for sample S2 as d_{Si} increases, and α_{sp} values remain

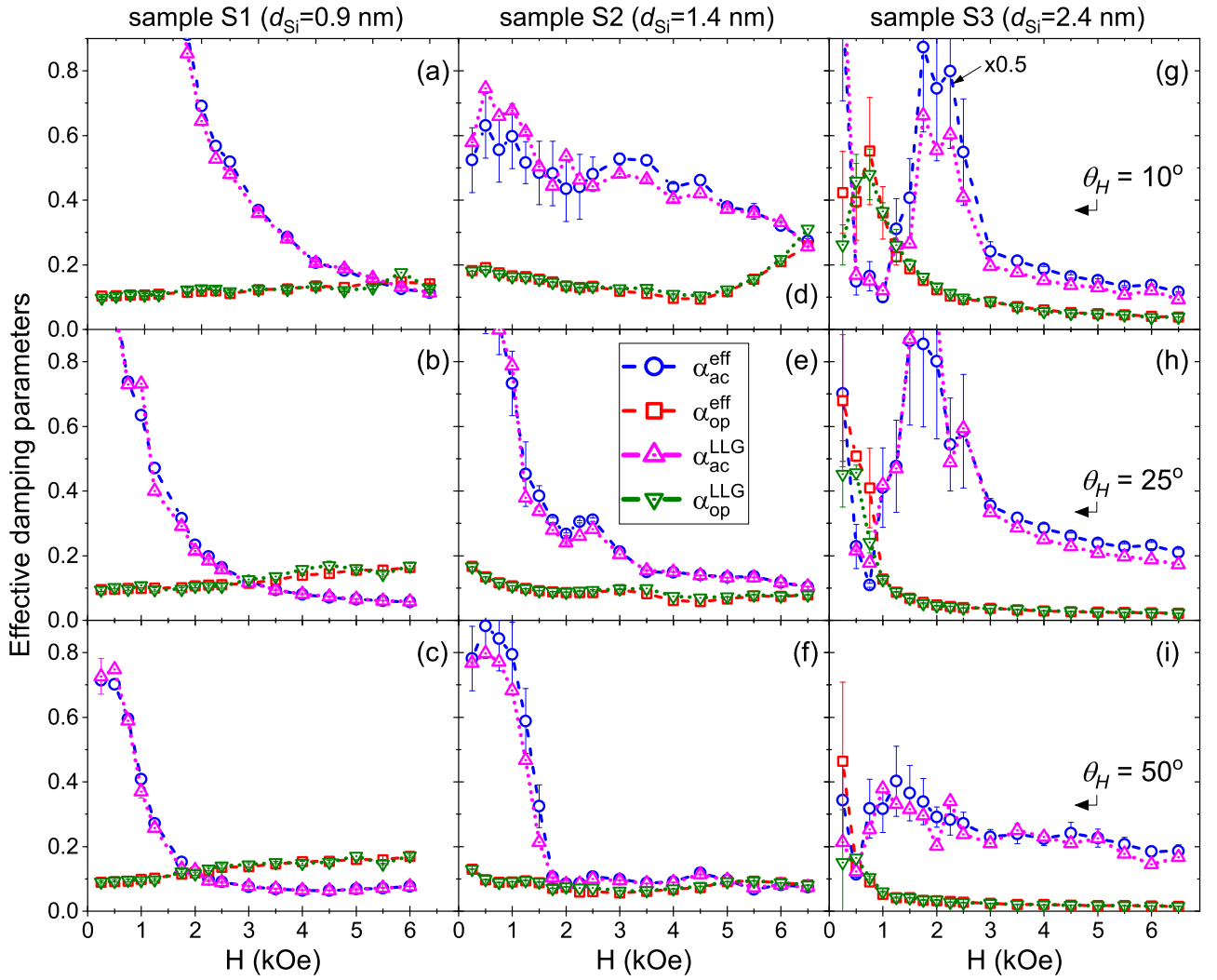


FIG. 5. Comparison of experimental $\alpha_{ac,op}^{eff}$ (blue and red symbols) and simulated with the use of LLG equations solutions effective damping parameters $\alpha_{ac,op}^{LLG}$ (magenta and green symbols) as a function of H and θ_H for acoustic and optic modes in Fe/Si(d_{Si}) multilayers for sample S1 [(a)–(c)], S2 [(d)–(f)], and S3 [(g)–(i)]. The experimental effective damping parameters were determined from the corresponding relaxation times, best fitted to experimental TRMOKE signals with the use of Eq. (18). The simulated damping parameters were determined in a similar way from the calculated LLG delay-time traces (see Sec. IV C 2).

approximately at the same level within the error bars for sample S3. The initial decreasing trend of α_{sp} with spacer-layer thickness was observed in Co-Fe/Ru/Co-Fe trilayers [62]. An interesting question can arise at this point concerning possible correlation occurrence between spin-pumping damping and interlayer exchange-coupling parameters. Such a correlation has been found in Ref. [62] between α_{sp} and effective coupling

parameter defined as $J_{eff} = J_1 + 2J_2$ in Co-Fe/Ru/Co-Fe trilayers. A similar correlation occurs in the case of Fe/Si MLS studied between α_{sp} and J_{eff} parameter defined as $|J_1| + 2J_2$.

(iii) The spin-mixing conductance parameter G_r calculated accordingly to Eq. (17e) has values in the range from $4.2 \times 10^{15} \Omega^{-1} m^{-2}$ for sample S2 to $7.3 \times 10^{15} \Omega^{-1} m^{-2}$ for sample S1 (see Table III). The obtained values are of the same

TABLE III. Parameters extracted from fitting of coupled LLG equation solutions to TRMOKE experimental data: intrinsic Gilbert damping α_0 and spin-pumping damping α_{sp} , and related parameters of the model used: real part of effective spin-mixing conductance parameter G_r and spin-diffusion length λ .

Sample	α_0	α_{sp}	G_r ($10^{15} \Omega^{-1} m^{-2}$)	λ (nm)
S1	0.061 ± 0.008	0.088 ± 0.008	7.3 ± 0.6	4.4 ± 0.7
S2	0.083 ± 0.018	0.067 ± 0.020	4.2 ± 1.3	5.1 ± 1.4
S3	0.013 ± 0.006	0.080 ± 0.035	6.8 ± 2.9	9.8 ± 2.8

order as reported for other systems. For example, the $G_r = 5.44 \times 10^{15} \Omega^{-1} \text{m}^{-2}$ was reported for CoFeB/Ru/CoFeB trilayers with strong antiferromagnetic BL coupling [49]. The changes of G_r values with d_{Si} can be related with differences in interface structural quality, as was reported for various layered structures [46].

(iv) The spin-diffusion length λ exhibits noticeable increasing trend with spacer-layer thickness. For smallest d_{Si} for samples S1 and S2, the $\lambda = 4.4 \pm 0.7 \text{ nm}$ and $5.1 \pm 1.4 \text{ nm}$ compare well with $\lambda = 5 \pm 1 \text{ nm}$ reported for Fe₃Si alloys [63,64]. For thickest d_{Si} for sample S3, the spin-diffusion length has a value increased to around 10 nm. Such an increase of λ can be probably related to the change of spacer-layer composition profile which was observed for similar sputter-deposited Fe/Si MLS [51].

In Fig. 5 we show results of simulation performed, aimed at comparison of experimental $\alpha_{\text{ac,op}}^{\text{eff}}$ (blue and red symbols) and simulated with the use of LLG equation solutions effective damping parameters $\alpha_{\text{ac,op}}^{\text{LLG}}$ (magenta and green symbols) as a function of H and θ_H for acoustic and optic modes in Fe/Si(d_{Si}) multilayers. The simulated effective $\alpha_{\text{ac}}^{\text{eff}}$ and $\alpha_{\text{op}}^{\text{eff}}$ parameters were determined from decompositions of theoretical delay-time traces (being the result of the fitting procedure of the LLG equations solutions to the experimental data) onto acoustic and optical mode contributions, performed in the way described in Sec. IV C 1.

As can be seen in Fig. 5, the simulated dependencies of effective damping parameters mostly coincide with experimental ones within error bars indicated. The overall good agreement of experimental and simulated effective damping parameters confirms the internal consistency of the adopted damping model and the calculation methodology used. However, several points are worth to be noticed and discussed. First, some discrepancies, mostly in low H fields, can be noted. Second, certain part of effective parameters obtained from the model can arise from contributions not included in LLG equations. One of the well-known sources of such contributions are magnetic inhomogeneities and two-magnon scattering, and both of them can have influence on the values of Gilbert damping as well as on spin-pumping damping parameter.

The inhomogeneity contribution can be separated already from effective α_{eff} parameters in the case of single magnetic layers, based on model analysis, as has been demonstrated in several papers [65–68]. In the simplest approach, the intrinsic part of α_{eff} was determined from the value at high H field, or from approximation to infinite field, where the contributions from the magnetic inhomogeneities, as well as from two-magnon scattering, tend to zero. However, this method does not apply to samples S1 and S2, where α_{eff} for optical mode tends to increase within the available magnetic field range.

Extrinsic enhancement of the damping can result also from two-magnon scattering processes, e.g., when the symmetry of the system is modified by inhomogeneity of microstructure such as film roughness and intermixing at interfaces [69–71], which enhance the effective damping of the magnetization precession. Increase of intermixing leads to the enhancement of effective spin-mixing conductance [71,72], and modifications of the interface can have influence on all of the mechanisms [73,74]. The contribution to the damping due to two-magnon scattering depends on the thickness of magnetic

layer as well as type and quality of interface with nonmagnetic layer, as has been determined for epitaxial Fe films with different capping layers by quantitative separation of intrinsic and extrinsic contributions in Refs. [75–77].

In Fe/Si multilayers two-magnon scattering can have influence on all parameters discussed so far. As already mentioned in Sec. IV B 2, Fe readily reacts with Si, forming a rich variety of silicides at the interfaces [32,34]. It was shown by Zakeri *et al.* in Refs. [78,79] that two-magnon scattering has significant effect on magnetic damping in Fe₃Si alloys. Similar influence of two-magnon scattering can be expected also for other compositions of Fe_xSi_{1-x} alloys, such as FeSi and FeSi₂, which are present in spacer-layer composition profiles in sputter-deposited Fe/Si MLS [51].

Investigation of influence of the inhomogeneity effects by introducing additional magnetic sublayers in the LLG equations and modeling of gradients of magnetic parameters at the interface volumes, or separation of two-magnon scattering contributions to the damping parameters, is however beyond the scope of this paper.

V. SUMMARY AND CONCLUSIONS

We performed comprehensive experimental and theoretical studies of the influence of coexisting bilinear (BL) and biquadratic (BQ) interlayer exchange coupling on magnetization precession in Fe(3 nm)/Si(d_{Si}) multilayers with different Si spacer-layer thicknesses d_{Si} and coupling strengths and signs. We studied laser-induced magnetization precession in the multilayers as a function of the magnitude H and orientation angle θ_H of external magnetic field using time-resolved magneto-optical Kerr effect. Strongly changing character of acoustic $\omega_{\text{ac}}(H, \theta_H)$ and optic $\omega_{\text{op}}(H, \theta_H)$ precession mode frequencies and effective damping parameter dependencies, determined for different d_{Si} thicknesses, varying in the range of 0.9–2.4 nm, has been observed.

Analytical formulas for acoustic and optic mode dispersion relations for the layered structures with coexisting bilinear and biquadratic interlayer couplings, scaled by J_1 and J_2 parameters, respectively, were derived for the case of in-plane effective magnetic anisotropy and arbitrary external magnetic field direction. It has been shown that for both modes, theoretical frequency dependencies reproduce very well the experimentally determined ones. It is shown that not only BL but also BQ IEC has significant influence on the shape and magnitude of $\omega_{\text{op,op}}(H, \theta_H)$ dispersion relations. In particular, nonmonotonic low-field frequency dependence of optical mode in the case of antiferromagnetic BL IEC is theoretically explained by the coexisting BQ IEC of similar strength. The acoustic and optic mode-crossing effect has been observed and accurately reproduced, with the crossing field and frequency gap values depending on coupling strengths and increasing as θ_H decreases. Similar BL and BQ IEC, of parameters values $J_1 \approx 1.6$ and $J_2 \approx 1.8 \text{ mJ/m}^2$ for spacer-layer thickness $d_{\text{Si}} = 0.9 \text{ nm}$ were found, while the BL IEC changes from ferromagnetic to antiferromagnetic coupling with $J_1 \approx -0.9 \text{ mJ/m}^2$ for $d_{\text{Si}} = 1.4 \text{ nm}$. It is shown that magnitudes of both coupling parameters decrease by one to two orders for $d_{\text{Si}} = 2.4 \text{ nm}$, which has large influence on the magnitude reduction, and form change of dispersion

relations of both frequency modes. It is found that the J_1 and J_2 parameters, determined in the dynamic TRMOKE and in the static MOKE experiments, and interpreted with the use of analytical formulas derived, coincide within the estimated error bars.

The description of the experimentally observed damping of magnetization precession was performed with the use of coupled LLG equation solutions within the model containing Gilbert damping and spin-pumping damping. In this model, the derived terms related to BQ IEC and spin-diffusion length in spin-pumping damping terms were taken into account. It is shown that the observed effective damping parameter dependencies on H and θ_H for acoustic and optic modes are very well simulated with the use of LLG equation solutions. The determined Gilbert damping, spin-pumping damping, and spin-diffusion length parameters were discussed in terms of possible extrinsic contributions from interface microstructure

inhomogeneities and two-magnon scattering. The Gilbert damping and spin-pumping-damping-related effective spin-mixing conductance of Fe/Si interfaces and spin-diffusion length parameters are found to be comparable with available data for other trilayer systems. The obtained accordance of simulated and experimental effective damping parameters confirms the internal consistency of the damping model and the calculation methodology used.

ACKNOWLEDGMENTS

Authors would like to thank T. Luciński and P. Chomiuk for providing samples for MOKE and TRMOKE measurements. The calculations were performed in part in Computational Centre of University in Białystok. This work was supported by the National Science Centre in Poland, Grant No. 2019/03/X/ST3/01500.

-
- [1] P. Grünberg, R. Schreiber, Y. Pang, M. B. Brodsky, and H. Sowers, Layered Magnetic Structures: Evidence for Antiferromagnetic Coupling of Fe Layers Across Cr Interlayers, *Phys. Rev. Lett.* **57**, 2442 (1986).
- [2] S. S. P. Parkin, Systematic Variation of the Strength and Oscillation Period of Indirect Magnetic Exchange Coupling Through the 3 d , 4 d , and 5 d Transition Metals, *Phys. Rev. Lett.* **67**, 3598 (1991).
- [3] M. D. Stiles, Interlayer exchange coupling, in *Ultrathin Magnetic Structures*, Volume III, edited by J. Anthony, C. Bland, and B. Heinrich, (Springer, Berlin, 2005), pp. 99–142.
- [4] Z. Zhang, L. Zhou, P. E. Wigen, and K. Ounadjela, Angular dependence of ferromagnetic resonance in exchange-coupled Co/Ru/Co trilayer structures, *Phys. Rev. B* **50**, 6094 (1994).
- [5] Z. Li, R. Skomski, S.-H. Liou, S. Michalski, M. Chipara, and R. D. Kirby, Magnetization precession and domain-wall structure in cobalt-ruthenium-cobalt trilayers, *J. Appl. Phys.* **109**, 07C113 (2011).
- [6] X. M. Liu, H. T. Nguyen, J. Ding, M. G. Cottam, and A. O. Adeyeye, Interlayer coupling in $\text{Ni}_{80}\text{Fe}_{20}/\text{Ru}/\text{Ni}_{80}\text{Fe}_{20}$ multilayer films: Ferromagnetic resonance experiments and theory, *Phys. Rev. B* **90**, 064428 (2014).
- [7] G. Wu, S. Chen, Y. Ren, Q. Y. Jin, and Z. Zhang, Laser-induced magnetization dynamics in interlayer-coupled $[\text{Ni}/\text{Co}]_4/\text{Ru}/[\text{Co}/\text{Ni}]_3$ perpendicular magnetic films for information storage, *ACS Appl. Nano Mater.* **2**, 5140 (2019).
- [8] C. Berk, F. Ganss, M. Jaris, M. Albrecht, and H. Schmidt, All-optical measurement of interlayer exchange coupling in Fe/Pt/FePt thin films, *Appl. Phys. Lett.* **112**, 052401 (2018).
- [9] P. Ogrodnik, J. Kanak, M. Czapkiewicz, S. Ziętek, A. Pietruczik, K. Morawiec, P. Dłużewski, K. Dybko, A. Wawro, and T. Stobiecki, Structural, magnetostatic, and magnetodynamic studies of Co/Mo-based uncompensated synthetic antiferromagnets, *Phys. Rev. Mater.* **3**, 124401 (2019).
- [10] A. Kamimaki, S. Iihama, K. Z. Suzuki, N. Yoshinaga, and S. Mizukami, Parametric Amplification of Magnons in Synthetic Antiferromagnets, *Phys. Rev. Appl.* **13**, 044036 (2020).
- [11] S. M. Rezende, C. Chesman, M. A. Lucena, A. Azevedo, F. M. de Aguiar, and S. S. P. Parkin, Studies of coupled metallic magnetic thin-film trilayers, *J. Appl. Phys.* **84**, 958 (1998).
- [12] Z. R. Nunn, C. Abert, D. Suess, and E. Girt, Control of the non-collinear interlayer exchange coupling, *Sci. Adv.* **6**, eabd8861 (2020).
- [13] S. Sorokin, R. A. Gallardo, C. Fowley, K. Lenz, A. Titova, G. Y. P. Atcheson, G. Dennehy, K. Rode, J. Fassbender, J. Lindner, and A. M. Deac, Magnetization dynamics in synthetic antiferromagnets: Role of dynamical energy and mutual spin pumping, *Phys. Rev. B* **101**, 144410 (2020).
- [14] Y. Ogasawara, Y. Sasaki, S. Iihama, A. Kamimaki, K. Z. Suzuki, and S. Mizukami, Laser-induced terahertz emission from layered synthetic magnets, *Appl. Phys. Express* **13**, 063001 (2020).
- [15] T. Kampfrath, M. Battiato, P. Maldonado, G. Eilers, J. Nötzold, S. Mährlein, V. Zbarsky, F. Freimuth, Y. Mokrousov, S. Blügel, M. Wolf, I. Radu, P. M. Oppeneer, and M. Münzenberg, Terahertz spin current pulses controlled by magnetic heterostructures, *Nat. Nanotechnol.* **8**, 256 (2013).
- [16] R. A. Duine, K.-J. Lee, S. S. P. Parkin, and M. D. Stiles, Synthetic antiferromagnetic spintronics, *Nat. Phys.* **14**, 217 (2018).
- [17] R. Mandal, D. Ogawa, Y. Tamazawa, K. Ishioka, T. Shima, T. Kato, S. Iwata, Y. Takahashi, S. Hirose, and K. Hono, Time domain magnetization dynamics study to estimate interlayer exchange coupling constant in Nd-Fe-B/ $\text{Ni}_{80}\text{Fe}_{20}$ films, *J. Magn. Magn. Mater.* **468**, 273 (2018).
- [18] A. Bonda, S. Uba, L. Uba, W. Skowroński, T. Stobiecki, and F. Stobiecki, Laser-induced magnetization precession parameters dependence on Pt spacer layer thickness in mixed magnetic anisotropies Co/Pt/Co trilayer, *J. Magn. Magn. Mater.* **505**, 166702 (2020).
- [19] J. Zhou, S. Saha, Z. Luo, E. Kirk, V. Scagnoli, and L. J. Heyderman, Ultrafast laser induced precessional dynamics in antiferromagnetically coupled ferromagnetic thin films, *Phys. Rev. B* **101**, 214434 (2020).
- [20] A. Layadi, Ferromagnetic resonance modes in single and coupled layers with oblique anisotropy axis, *Phys. Rev. B* **63**, 174410 (2001).
- [21] A. Layadi, Effect of biquadratic coupling and in-plane anisotropy on the resonance modes of a trilayer system, *Phys. Rev. B* **65**, 104422 (2002).

- [22] A. Layadi and J. Artman, Ferromagnetic resonance in a coupled two-layer system, *J. Magn. Magn. Mater.* **92**, 143 (1990).
- [23] B. Khodadadi, J. B. Mohammadi, J. M. Jones, A. Srivastava, C. Mewes, T. Mewes, and C. Kaiser, Interlayer Exchange Coupling in Asymmetric Co–Fe/Ru/Co–Fe Trilayers Investigated with Broadband Temperature-Dependent Ferromagnetic Resonance, *Phys. Rev. Appl.* **8**, 014024 (2017).
- [24] A. Sud, C. W. Zollitsch, A. Kamimaki, T. Dion, S. Khan, S. Iihama, S. Mizukami, and H. Kurebayashi, Tunable magnon-magnon coupling in synthetic antiferromagnets, *Phys. Rev. B* **102**, 100403(R) (2020).
- [25] A. Kirilyuk, A. V. Kimel, and T. Rasing, Ultrafast optical manipulation of magnetic order, *Rev. Mod. Phys.* **82**, 2731 (2010).
- [26] B. Zhao, H. Xue, G. Wu, Z. Zhu, Y. Ren, Q. Y. Jin, and Z. Zhang, Interlayer modulation on the dynamic magnetic properties of $L1_0$ -FePt/NM/[CoNi]₅ composite film structures, *Appl. Phys. Lett.* **115**, 062401 (2019).
- [27] G. J. Strijkers, J. T. Kohlhepp, H. J. M. Swagten, and W. J. M. de Jonge, Origin of Biquadratic Exchange in Fe/Si/Fe, *Phys. Rev. Lett.* **84**, 1812 (2000).
- [28] Y. Endo, O. Kitakami, and Y. Shimada, Interlayer coupling of Fe/Si/Fe trilayers with very thin boundary layers, *J. Appl. Phys.* **85**, 5741 (1999).
- [29] G. J. Strijkers, J. T. Kohlhepp, H. J. M. Swagten, and W. J. M. de Jonge, Biquadratic interlayer exchange coupling in epitaxial Fe/Si/Fe, *J. Appl. Phys.* **87**, 5452 (2000).
- [30] R. Gareev, D. Bürgler, M. Buchmeier, R. Schreiber, and P. Grünberg, Very strong interlayer exchange coupling in epitaxial Fe/Fe_{1-x}Si_x/Fe trilayers ($x = 0.4 - 1.0$), *J. Magn. Magn. Mater.* **240**, 235 (2002).
- [31] B. K. Kuanr, M. Buchmeier, D. E. Buegler, P. Gruenberg, R. Camley, and Z. Celinski, Dynamic and static measurements on epitaxial Fe/Si/Fe, *J. Vac. Sci. Technol. A* **21**, 1157 (2003).
- [32] B. Croonenborghs, F. M. Almeida, C. L'abbé, R. R. Gareev, M. Rots, A. Vantomme, and J. Meersschaet, Interlayer coupling across semimetallic iron monosilicide, *Phys. Rev. B* **71**, 024410 (2005).
- [33] J. Bartolomé, L. Badía-Romano, J. Rubín, F. Bartolomé, S. Varnakov, S. Ovchinnikov, and D. Bürgler, Magnetic properties, morphology and interfaces of (Fe/Si)_n nanostructures, *J. Magn. Magn. Mater.* **400**, 271 (2016).
- [34] A. Kumar, R. Brajpuriya, and P. Singh, Study of ion beam sputtered Fe/Si interfaces as a function of Si layer thickness, *J. Appl. Phys.* **123**, 025305 (2018).
- [35] F. Stromberg, S. Bedanta, C. Antoniak, W. Keune, and H. Wende, FeSi diffusion barriers in Fe/FeSi/Si/FeSi/Fe multilayers and oscillatory antiferromagnetic exchange coupling, *J. Phys.: Condens. Matter* **20**, 425205 (2008).
- [36] A. Bonda, L. Uba, K. Załęski, and S. Uba, Ultrafast magnetization dynamics in an epitaxial Ni_{54.3}Mn_{31.9}Sn_{13.8} Heusler-alloy film close to the Curie temperature, *Phys. Rev. B* **99**, 184424 (2019).
- [37] A. Bonda, S. Uba, K. Załęski, J. Dubowik, and L. Uba, Ultrafast magnetization dynamics in epitaxial Ni-Mn-Sn Heusler alloy film, *Acta Phys. Pol. A* **133**, 501 (2018).
- [38] A. N. Yaresko, L. Uba, S. Uba, A. Y. Perlov, R. Gontarz, and V. N. Antonov, Magneto-optical Kerr spectroscopy of palladium, *Phys. Rev. B* **58**, 7648 (1998).
- [39] S. Uba, L. Uba, R. Gontarz, V. Antonov, A. Perlov, and A. Yaresko, Experimental and theoretical study of the magneto-optical properties of CoPt multilayers, *J. Magn. Magn. Mater.* **140-144**, 575 (1995).
- [40] L. Uba, A. Bonda, S. Uba, L. V. Bekenov, and V. N. Antonov, Electronic structure and magneto-optical Kerr spectra of an epitaxial Ni_{54.3}Mn_{31.9}Sn_{13.8} Heusler alloy film, *J. Phys.: Condens. Matter* **29**, 275801 (2017).
- [41] P. Chomiuk, M. Błaszzyk, B. Szymański, and T. Luciński, Interface mixing in Fe/Si multilayers observed by the in situ conductance measurements, *Acta Phys. Pol. A* **115**, 355 (2009).
- [42] P. Chomiuk, M. Wróblewski, M. Błaszzyk, T. Luciński, and B. Susła, In situ conductance of Fe/Si and Fe/Ge multilayers, *Acta Phys. Pol. A* **113**, 657 (2008).
- [43] C. Eyrieh, A. Zamani, W. Huttema, M. Arora, D. Harrison, F. Rashidi, D. Broun, B. Heinrich, O. Mryasov, M. Ahlberg, O. Karis, P. E. Jönsson, M. From, X. Zhu, and E. Girt, Effects of substitution on the exchange stiffness and magnetization of Co films, *Phys. Rev. B* **90**, 235408 (2014).
- [44] Y. Tserkovnyak, A. Brataas, G. E. W. Bauer, and B. I. Halperin, Nonlocal magnetization dynamics in ferromagnetic heterostructures, *Rev. Mod. Phys.* **77**, 1375 (2005).
- [45] T. Chiba, G. E. W. Bauer, and S. Takahashi, Magnetization damping in noncollinear spin valves with antiferromagnetic interlayer couplings, *Phys. Rev. B* **92**, 054407 (2015).
- [46] C. J. Durrant, L. R. Shelford, R. A. J. Valkass, R. J. Hicken, A. I. Figueroa, A. A. Baker, G. van der Laan, L. B. Duffy, P. Shafer, C. Klewe, E. Arenholz, S. A. Cavill, J. R. Childress, and J. A. Katine, Dependence of spin pumping and spin transfer torque upon Ni₈₁Fe₁₉ thickness in Ta/Ag/Ni₈₁Fe₁₉/Ag/Co₂MnGe/Ag/Ta spin-valve structures, *Phys. Rev. B* **96**, 144421 (2017).
- [47] R. Medwal, S. Gupta, R. S. Rawat, A. Subramanian, and Y. Fukuma, Spin pumping in asymmetric Fe₅₀Pt₅₀/Cu/Fe₂₀Ni₈₀ trilayer structure, *Phys. Status Solidi RRL* **13**, 1900267 (2019).
- [48] Y. Li, W. Cao, V. P. Amin, Z. Zhang, J. Gibbons, J. Sklenar, J. Pearson, P. M. Haney, M. D. Stiles, W. E. Bailey, V. Novosad, A. Hoffmann, and W. Zhang, Coherent Spin Pumping in a Strongly Coupled Magnon-Magnon Hybrid System, *Phys. Rev. Lett.* **124**, 117202 (2020).
- [49] A. Kamimaki, S. Iihama, T. Taniguchi, and S. Mizukami, All-optical detection and evaluation of magnetic damping in synthetic antiferromagnet, *Appl. Phys. Lett.* **115**, 132402 (2019).
- [50] Y. Pogoryelov, M. Pereiro, S. Jana, A. Kumar, S. Akansel, M. Ranjbar, D. Thonig, D. Primetzhofer, P. Svedlindh, J. Åkerman, O. Eriksson, O. Karis, and D. A. Arena, Nonreciprocal spin pumping damping in asymmetric magnetic trilayers, *Phys. Rev. B* **101**, 054401 (2020).
- [51] T. Luciński and P. Chomiuk, Magnetic and electric properties of (Fe, Co)/(Si, Ge) multilayers, *Open Phys.* **9**, 276 (2011).
- [52] D. MacNeill, J. T. Hou, D. R. Klein, P. Zhang, P. Jarillo-Herrero, and L. Liu, Gigahertz Frequency Antiferromagnetic Resonance and Strong Magnon-Magnon Coupling in the Layered Crystal CrCl₃, *Phys. Rev. Lett.* **123**, 047204 (2019).
- [53] M. Ishibashi, Y. Shiota, T. Li, S. Funada, T. Moriyama, and T. Ono, Switchable giant nonreciprocal frequency shift of propagating spin waves in synthetic antiferromagnets, *Sci. Adv.* **6**, eaaz6931 (2020).
- [54] H. J. Waring, N. A. B. Johansson, I. J. Vera-Marun, and T. Thomson, Zero-Field Optic Mode Beyond 20 GHz in a Synthetic Antiferromagnet, *Phys. Rev. Appl.* **13**, 034035 (2020).

- [55] A. Sud, Y. Koike, S. Iihama, C. Zollitsch, S. Mizukami, and H. Kurebayashi, Parity-controlled spin-wave excitations in synthetic antiferromagnets, *Appl. Phys. Lett.* **118**, 032403 (2021).
- [56] J. C. Slonczewski, Origin of biquadratic exchange in magnetic multilayers (invited), *J. Appl. Phys.* **73**, 5957 (1993).
- [57] S. N. Varnakov, S. V. Komogortsev, S. G. Ovchinnikov, J. Bartolomé, and J. Sesé, Magnetic properties and nonmagnetic phases formation in $(\text{Fe}/\text{Si})_n$ films, *J. Appl. Phys.* **104**, 094703 (2008).
- [58] C. Dai and F. Ma, Strong magnon-magnon coupling in synthetic antiferromagnets, *Appl. Phys. Lett.* **118**, 112405 (2021).
- [59] X. Chen, C. Zheng, S. Zhou, Y. Liu, and Z. Zhang, Manipulation of time- and frequency-domain dynamics by magnon-magnon coupling in synthetic antiferromagnets, *Magnetochemistry* **8**, 7 (2022).
- [60] S. Mizukami, K. Z. Suzuki, and Y. Miura, All-optical probe of sub-THz spin precession in a $L1_0$ MnGa nanolayer, *Appl. Phys. Express* **12**, 043003 (2019).
- [61] A. Bonda, S. Uba, L. Uba, and J. Dubowik, Influence of magnetic field orientation on laser-induced magnetization precession in Ni-Mn-Sn Heusler alloy film, *J. Magn. Magn. Mater.* **504**, 166686 (2020).
- [62] Y. Zhang, G. Wu, Z. Ji, X. Chen, Q. Y. Jin, and Z. Zhang, Significant and Nonmonotonic Dynamic Magnetic Damping in Asymmetric Co-Fe/Ru/Co-Fe Trilayers, *Phys. Rev. Appl.* **17**, 034033 (2022).
- [63] K. Hamaya, N. Hashimoto, S. Oki, S. Yamada, M. Miyao, and T. Kimura, Estimation of the spin polarization for Heusler-compound thin films by means of nonlocal spin-valve measurements: Comparison of Co_2FeSi and Fe_3Si , *Phys. Rev. B* **85**, 100404(R) (2012).
- [64] K. Tanikawa, S. Oki, S. Yamada, K. Mibu, M. Miyao, and K. Hamaya, Effect of Co-Fe substitution on room-temperature spin polarization in $\text{Co}_{3-x}\text{Fe}_x\text{Si}$ Heusler-compound films, *Phys. Rev. B* **88**, 014402 (2013).
- [65] S. Iihama, S. Mizukami, H. Naganuma, M. Oogane, Y. Ando, and T. Miyazaki, Gilbert damping constants of Ta/CoFeB/MgO(Ta) thin films measured by optical detection of precessional magnetization dynamics, *Phys. Rev. B* **89**, 174416 (2014).
- [66] S. Iihama, A. Sakuma, H. Naganuma, M. Oogane, S. Mizukami, and Y. Ando, Influence of $L1_0$ order parameter on Gilbert damping constants for FePd thin films investigated by means of time-resolved magneto-optical Kerr effect, *Phys. Rev. B* **94**, 174425 (2016).
- [67] A. Capua, S.-h. Yang, T. Phung, and S. S. P. Parkin, Determination of intrinsic damping of perpendicularly magnetized ultrathin films from time-resolved precessional magnetization measurements, *Phys. Rev. B* **92**, 224402 (2015).
- [68] D. M. Lattery, D. Zhang, J. Zhu, X. Hang, J.-P. Wang, and X. Wang, Low Gilbert damping constant in perpendicularly magnetized W/CoFeB/MgO films with high thermal stability, *Sci. Rep.* **8**, 13395 (2018).
- [69] M. J. Hurben and C. E. Patton, Theory of two magnon scattering microwave relaxation and ferromagnetic resonance linewidth in magnetic thin films, *J. Appl. Phys.* **83**, 4344 (1998).
- [70] E. Barati, M. Cinal, D. M. Edwards, and A. Umerski, Gilbert damping in magnetic layered systems, *Phys. Rev. B* **90**, 014420 (2014).
- [71] S. Azzawi, A. Ganguly, M. Tokaç, R. M. Rowan-Robinson, J. Sinha, A. T. Hindmarch, A. Barman, and D. Atkinson, Evolution of damping in ferromagnetic/nonmagnetic thin film bilayers as a function of nonmagnetic layer thickness, *Phys. Rev. B* **93**, 054402 (2016).
- [72] Y. Liu, Z. Yuan, R. J. H. Wesselink, A. A. Starikov, and P. J. Kelly, Interface Enhancement of Gilbert Damping from First Principles, *Phys. Rev. Lett.* **113**, 207202 (2014).
- [73] J. A. King, A. Ganguly, D. M. Burn, S. Pal, E. A. Sallabank, T. P. A. Hase, A. T. Hindmarch, A. Barman, and D. Atkinson, Local control of magnetic damping in ferromagnetic/nonmagnetic bilayers by interfacial intermixing induced by focused ion-beam irradiation, *Appl. Phys. Lett.* **104**, 242410 (2014).
- [74] A. Ganguly, S. Azzawi, S. Saha, J. A. King, R. M. Rowan-Robinson, A. T. Hindmarch, J. Sinha, D. Atkinson, and A. Barman, Tunable magnetization dynamics in interfacially modified $\text{Ni}_{81}\text{Fe}_{19}/\text{Pt}$ bilayer thin film microstructures, *Sci. Rep.* **5**, 17596 (2015).
- [75] G. Woltersdorf, M. Buess, B. Heinrich, and C. H. Back, Time Resolved Magnetization Dynamics of Ultrathin Fe(001) Films: Spin-Pumping and Two-Magnon Scattering, *Phys. Rev. Lett.* **95**, 037401 (2005).
- [76] A. Conca, S. Keller, M. R. Schweizer, E. T. Papaioannou, and B. Hillebrands, Separation of the two-magnon scattering contribution to damping for the determination of the spin mixing conductance, *Phys. Rev. B* **98**, 214439 (2018).
- [77] Z. Xu, K. Zhang, and J. Li, Disentangling intrinsic and extrinsic Gilbert damping, *Phys. Rev. B* **104**, 224404 (2021).
- [78] K. Zakeri, J. Lindner, I. Barsukov, R. Meckenstock, M. Farle, U. von Hörsten, H. Wende, W. Keune, J. Rucker, S. S. Kalarickal, K. Lenz, W. Kuch, K. Baberschke, and Z. Frait, Spin dynamics in ferromagnets: Gilbert damping and two-magnon scattering, *Phys. Rev. B* **76**, 104416 (2007).
- [79] K. Zakeri, J. Lindner, I. Barsukov, R. Meckenstock, M. Farle, U. von Hörsten, H. Wende, W. Keune, J. Rucker, S. S. Kalarickal, K. Lenz, W. Kuch, K. Baberschke, and Z. Frait, Erratum: Spin dynamics in ferromagnets: Gilbert damping and two-magnon scattering [Phys. Rev. B 76, 104416 (2007)], *Phys. Rev. B* **80**, 059901(E) (2009).